ResearchGate

See discussions, stats, and author profiles for this publication at: https://www.researchgate.net/publication/368414604

Late Holocene temperature and precipitation variations in an alpine region of the northeastern Tibetan Plateau and their response to global climate change

Article *in* Palaeogeography Palaeoclimatology Palaeoecology · February 2023

DOI: 10.1016/j.palaeo.2023.111442

CITATIONS
0

READS
315

6 authors, including:

Youmo Li
Lanzhou University
7 PUBLICATIONS **15** CITATIONS

SEE PROFILE

Duo Wu
Lanzhou University
68 PUBLICATIONS **1,109** CITATIONS

SEE PROFILE

Lin Chen
Lanzhou University
10 PUBLICATIONS **45** CITATIONS

SEE PROFILE

Some of the authors of this publication are also working on these related projects:

Project General Financial Grant from the China Postdoctoral Science Foundation (No. 2017M623272) View project

Project Historical background of the Anthropocene View project

All content following this page was uploaded by Duo Wu on 16 February 2023.

The user has requested enhancement of the downloaded file.

Palaeogeography, Palaeoclimatology, Palaeoecology 615 (2023) 111442

Contents lists available at ScienceDirect

Palaeogeography, Palaeoclimatology, Palaeoecology

journal homepage: www.elsevier.com/locate/palaeo

Late Holocene temperature and precipitation variations in an alpine region of the northeastern Tibetan Plateau and their response to global climate change

Youmo Li [a], Duo Wu [a,*], Tao Wang [a], Lin Chen [a], Chenbin Zhang [b], Shilong Guo [a]

[a] Key Laboratory of Western China's Environmental Systems (Ministry of Education), College of Earth and Environmental Sciences, Lanzhou University, Lanzhou 730000, China

[b] Alpine Paleoecology and Human Adaptation Group (ALPHA), Institute of Tibetan Plateau Research, Chinese Academy of Sciences, Beijing 100101, China

ARTICLE INFO

Editor: Dr. Howard Falcon-Lang

Keywords:
Northeastern Tibetan Plateau
Alpine lake
Temperature–precipitation reconstruction
Late Holocene
Climatic forcing
Global climate teleconnection

ABSTRACT

Knowledge of temperature and precipitation variations on the northeastern Tibetan Plateau (NETP) during the recent past can improve our understanding of late Holocene regional climate change and its response to global climate change, in the past and potentially the future. Based on records of multiple geochemical indicators and branched glycerol dialkyl glycerol tetraethers from the sediments of alpine Lake Bihu on the NETP, we reconstructed high-resolution precipitation sequences and quantified the variation of the mean air temperature of months above freezing (MAF, between May and October) over the past ~3500 years. The MAF reconstruction shows obvious fluctuations on decadal to centennial timescales, and the absolute values of the reconstructed temperature range from 0.70 to 3.98 °C, with an average of 2.19 °C. The precipitation record reflects the high-frequency variability of the East Asian summer monsoon (EASM). The maximum precipitation and temperature on the NETP occurred during the Medieval Warm Period (MWP, ~800–1400 CE), rather than during the Current Warm Period (CWP, the last 150 years). We also observed broadly similar patterns of warm–wet and cold–dry climatic variations over the NETP and the broader EASM region; moreover, the decadal to centennial temperature fluctuations were consistent on a large spatial scale. Our results indicate that temperature variability during the late Holocene was primarily controlled by solar radiation, interrupted by multiple decades of successive volcanic eruptions. In addition, anomalous and rapid warming during the CWP may also be related to the unprecedented increase in atmospheric greenhouse gases. Precipitation variability in this region, driven by changes in the EASM, may have been primarily a response to changes in total solar irradiance and associated changes in atmospheric–oceanic modes (e.g., the El Niño–Southern Oscillation, Intertropical Convergence Zone, and Western Pacific Subtropical High). Overall, our results provide robust evidence for global climate teleconnections between different regions, especially in high mountains, in the past, present, and potentially in the future.

1. Introduction

Global warming is expected to amplify a hydrological imbalance on the Tibetan Plateau, also known as the "Asian water tower", caused by the accelerated transformation of ice and snow into liquid water (Immerzeel et al., 2010; Yao et al., 2022). The Tibetan Plateau has experienced substantial recent warming, evidenced by observation data from meteorological stations beginning in the mid-1950s (Liu and Chen, 2000). In recent decades the annual temperature over the Tibetan Plateau has increased twice as fast as the global average (Chylek et al., 2009; Chen et al., 2015a), and this regional warming rate since the 1980s is unparalleled over the past two millennia (Chylek et al., 2009; Yao et al., 2019; Yan et al., 2020; Zhang et al., 2020; You et al., 2021). The northeastern Tibetan Plateau (NETP) is especially sensitive to climate change, given its location on the edge of the subtropical Asia monsoon circulations, and it may act as a link between high- and low-latitude climatic processes in the Northern Hemisphere (Ding and Wang., 2005; Chen et al., 2010).

During the past few decades numerous studies have been conducted involving modern climate observations and paleoclimate reconstruction on increasingly long timescales, especially for the late Holocene, with the aim of predicting future climatic changes across the ecologically

* Corresponding author.
E-mail address: dwu@lzu.edu.cn (D. Wu).

https://doi.org/10.1016/j.palaeo.2023.111442
Received 4 November 2022; Received in revised form 4 February 2023; Accepted 6 February 2023
Available online 9 February 2023
0031-0182/© 2023 Elsevier B.V. All rights reserved.

fragile NETP. It has been found that several periods of distinct temperature fluctuations have occurred on a centennial timescale, with a series of abrupt climatic events occurring during the late Holocene; they include the Roman Warm Period (RWP, ~250–450 CE, Common Era), Dark Ages Cold Period (DACP, ~450–800 CE), Medieval Warm Period (MWP, ~800–1400 CE), Little Ice Age (LIA, ~1400–1800 CE), and Current Warm Period (CWP; since ~1850 CE) (Moberg et al., 2005; Ljungqvist, 2010; Ge et al., 2010, 2013; Diaz et al., 2011; Chen et al., 2015b; PAGES 2k Consortium, 2017; Feng et al., 2019; Lan et al., 2020). The climate of the MWP was like that during the CWP, and thus it provides a reference frame for evaluating the possible future precipitation response to ongoing climatic warming (Diaz et al., 2011).

Temperature is generally spatially consistent on a large spatial scale. However, recent studies have revealed significant contradictions between temperatures reconstructed using paleoclimatic records and climate simulations during the Holocene (Marcott et al., 2013; Liu et al., 2014; Brierley et al., 2020). Therefore, the long-term trend of temperature fluctuations during the late Holocene is still debated. In contrast to temperature records, there is notable spatial heterogeneity in reconstructed hydroclimatic records across the NETP and its surrounding areas, over the last ~3500 years (Yang et al., 2003; Zhang et al., 2003a; Chen et al., 2006; Liu et al., 2006; He et al., 2013a; Yang et al., 2014; An et al., 2018; Wu et al., 2020, 2022). Moreover, numerous paleoclimatic studies have revealed significant differences in regional climatic patterns across the NETP, where the climate was influenced by interactions between the westerlies and the East Asian summer monsoon (EASM) during the late Holocene (Tian et al., 2001; Yang et al., 2003, 2014, 2021; Zhang et al., 2003b; Chen et al., 2006, 2010; Liu et al., 2006; Zhang et al., 2008; He et al., 2013a). For example, the Sugan Lake and Gahai Lake areas on the NETP were affected by the interaction between the mid-latitude westerlies circulation and the EASM, and they experienced a warm–dry MWP and cold–humid LIA (He et al., 2013a; Yao et al., 2013; Chen et al., 2016; Lan et al., 2020). In contrast, the Dunde, Delingha and Dulan areas, in the southeastern Qilian Mountains, and the Lake Qinghai basin, were influenced solely by the EASM and experienced a warm–humid MWP and cold–dry LIA (Yang et al., 2003; Zhang et al., 2003b; Liu et al., 2006; Yang et al., 2014, 2021).

Although a series of relevant paleoclimatic studies have been undertaken in recent decades, the contradictions in the hydrothermal configuration on the NETP during the climatic periods mentioned above, and the driving forces behind the natural variability, remain poorly understood (Yang et al., 2003, 2014; Zhang et al., 2003b; Liu et al., 2006). In addition, there is a lack of high-resolution hydroclimatic and quantitative temperature reconstructions with an independent chronology obtained from the same core, resulting in a heavy reliance on the accuracy of sedimentary age models; hence, the various late Holocene paleoclimate studies of the Tibetan Plateau cannot directly be compared without taking chronological uncertainties into account. Therefore, additional and reliable paleotemperature and hydroclimatic reconstructions are needed to improve our understanding of the mechanisms of climate change across the NETP during the late Holocene.

Previous studies have shown that the distribution of branched glycerol dialkyl glycerol tetraethers (brGDGTs) is related to environmental factors, including mean annual air temperature (MAAT) and soil pH (Weijers et al., 2007; Peterse et al., 2012; De Jonge et al., 2014; Dang et al., 2018; Russell et al., 2018). This is the result of bacteria producing more/less methyl branches to adjust to colder/warmer conditions, and thus quantitative functions based on the methylation of branched tetraether (MBT) index between brGDGT distributions and temperature have been proposed as a novel proxy for using in terrestrial settings (e.g., in soils and lakes) across the Tibetan Plateau (Wu et al., 2013; Günther et al., 2014; Ding et al., 2015; Wang et al., 2015a, 2016a, 2021; Li et al., 2017, 2019; Feng et al., 2019, 2022; He et al., 2020; Zhao et al., 2021; Sun et al., 2021; Zhang et al., 2022a) and other regions (De Jonge et al., 2014; Dang et al., 2018; Russell et al., 2018). Additionally, Lake Bihu, an alpine lake with continuous and high-resolution sedimentary strata, contains abundant lipids, and thus it is regarded as an ideal archive for investigating temperature changes on the NETP during the late Holocene. However, in high-altitude regions, lake water temperature reconstructed from sedimentary brGDGTs may not reflect the true atmospheric temperature during the freezing season, because the water in alpine lakes cannot fully exchange heat with the atmosphere when the lake surface is frozen. Which hinders brGDGTs-based air temperature reconstruction. During the ice-free season, the mean air temperature of the months above freezing (MAF, between May and October) of lake water is close to that of the atmosphere; moreover, there is the abundant production of brGDGTs from bacteria in the lake during this period, and thus the temperature reconstructed by brGDGTs can reliably represent the local atmospheric temperature (Sun et al., 2021; Raberg et al., 2021; Zhang et al., 2021, 2022a).

Consequently, the aims of the present study are as follows. 1) To quantitatively reconstruct the MAF during the late Holocene (the last 3500 years), and to compare it with the instrumental temperature record from a high-elevation site on the NETP, based on the brGDGTs data from a sediment core from Lake Bihu. 2) To reconstruct high-resolution summer monsoon precipitation changes from the same core spanning the same interval, using multiple geochemical proxies, including X-ray fluorescence (XRF)-based elements, grain size, loss-on-ignition (LOI), and sedimentary mineralogy. 3) To elucidate the climatic patterns over the NETP and their possible forcing mechanisms on decadal to centennial timescales during the late Holocene, based on a comparison of our results with previously published paleoclimatic records, as well with climate forcing factors.

2. Regional setting

Lake Bihu (35°30′28.61″ – 35°30′29.10″ N, 102°40′52.84″ – 102°40′54.06″ E; 4360 m a.s.l.) is located within the southwestern Dalijia Mountains, a transitional region between the NETP and the Chinese Loess Plateau (Fig. 1a, b). The average elevation of the Dalijia Mountains is ~3600 m a.s.l., with Dalijia Peak reaching 4636 m a.s.l. Lake Bihu is located on a planation surface between 4000 and 4400 m a.s.l., at higher levels in the Dalijia Mountains (Wang et al., 2013). The topography of this region is complex and there are valleys to both the west (Qitai valley) and east (Deheisui valley), which intersect and converge to the south. There are no glaciers in this area at the present-day, but during the Quaternary the area was intensively and repeatedly glaciated, and numerous well-preserved moraines were formed (Li and Pan, 1989; Shen et al., 1989; Pan, 1993; Wang et al., 2013). The bedrock around the lake consists mainly of intensely folded and faulted Precambrian crystalline complexes of granite and schist (Wang et al., 2015b). The geological structure is characterized by deformation, which is mainly the result of late Neogene orogenic events (Mahaney and Rutter, 1992). Field surveys and remote sensing images show that the surrounding landscape is alpine meadow and alpine grassland. The region has a temperate semi-arid continental climate, with dry and cold conditions during winter and spring, and wet and warm conditions during summer and autumn. Moisture in this region is derived mainly from the EASM in summer, and transported by the westerlies in winter, on both seasonal and interdecadal timescales (Yao et al., 2012, 2013; Ma et al., 2022). At Linxia Station (35°34′ N, 103°11′ E; 1917 m a.s.l.), ~40 km from the eastern slopes of Dalijia Shan Peak, a MAAT of 7.23 °C, MAF of 14.59 °C, and mean annual precipitation (MAP) of 418 mm were reported during 1951–2020 CE, and precipitation between May and October accounts for >85% of the annual total (Fig. 1c).

Lake Bihu and its surroundings were occupied by an ice cap during the middle of Marine Oxygen Isotope Stage 3, the oldest glacial advance event; subsequently, the range of glaciers retreated below 4300 m, and a small, closed lake was formed following glacial retreat and erosion (Li and Pan, 1989; Pan, 1993; Wang et al., 2013). Today, Lake Bihu is a small, semi-open lake and its water is primarily supplied by precipitation during the rainy summers. The water overflows from the outlet

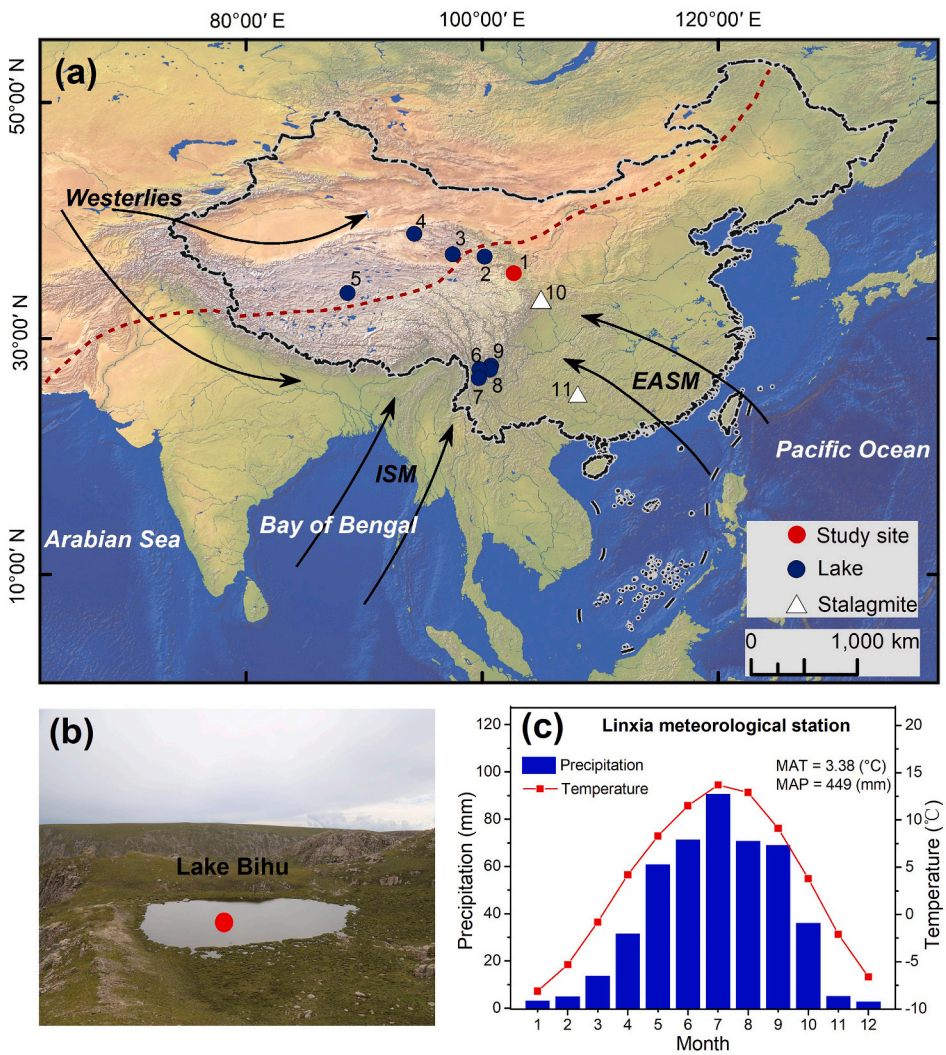

Fig. 1. Map showing the location and climate of the study area. (a) Locations of Lake Bihu and the cited paleoclimatic records on the Tibetan Plateau and the surrounding region (1: Lake Bihu, 2: Lake Qinghai, 3: Lake Gahai, 4: Lake Sugan, 5: Linggo Co, 6: Lake Cuoqia, 7: Lake Tiancai, 8: Lake Heihai, 9: Lake Lugu, 10: Wangxiang Cave, 11: Dongge Cave). Filled circles and triangles denote lake and stalagmite records, respectively. Black arrows show the regional atmospheric circulation (Westerlies, Indian summer monsoon (ISM), and East Asian summer monsoon (EASM)) (Yao et al., 2013). The red dotted line shows the modern limit of the Asian summer monsoon (ASM; modified from Chen et al. (2010)). (b) Lake surface extent and sampling site. (c) Monthly mean precipitation and temperature recorded at Linxia Meteorological Station (1951–2020) (http://data.cma.cn). (For interpretation of the references to colour in this figure legend, the reader is referred to the web version of this article.)

when the maximum water depth exceeds 5.7 m, while the lake surface is ice-covered from November to April. The lake covers an area of ~13,000 m^2, and its catchment area is ~0.02 km^2.

The ecosystem of this piedmont basin has been influenced by human activity, including agricultural practices, beginning with settlement in the 11th century (Zhang et al., 2022b), and intensified grazing (mainly by yaks and sheep) has occurred in the catchment of Lake Bihu and the surrounding areas during the last few decades. Additionally, several ancient settlements were built on the flat and gentle slopes of the Ganjia Basin (Xia et al., 2020).

3. Materials and methods

3.1. Materials

In September 2020, a 218-cm-long core (BH20) was obtained from the center of Lake Bihu (water depth of 5.7 m; see Fig. 1b for the site location), using a Livingstone corer. The core was collected in half-section polyethylene tubes and transported to the laboratory, where it was stored at 4 °C prior to analysis. Core BH20 core was split vertically and one half was used for XRF analysis. The other half was sub-sampled at 0.5 cm intervals and the samples were freeze-dried for various other laboratory analyses. One surface soil sample was obtained from the lake catchment and two loess samples were collected from the Ganjia Basin (the piedmont basin in the study area).

3.2. Methods

3.2.1. Dating

The ages of selected samples from core BH20 were determined by accelerator mass spectrometry (AMS) ^{14}C dating. Six samples of bulk organic matter from different depths (Table 1) were treated with standard acid–base–acid preparational procedures following (Olsson, 1986), and ^{14}C analysis was conducted by Beta Analytic (Florida, USA). The 'intercept method' based on least-squares fitting was used to evaluate the possible influence of the old carbon effect on the sediments of Lake Bihu. Subsequently, the radiocarbon ages (after calibration for the carbon reservoir effect) were calibrated to calendar years before present (yr BP, where the present is defined as the year 1950 CE) using the CALIB 8.0.1 program. Finally, an age–depth model, including the age uncertainty, was developed using R software, implemented by the Clam library (Blaauw, 2010) with the IntCal 20 calibration curve (Reimer et al., 2020).

3.2.2. Geochemistry and grain-size analyses

After covering its surface with Ultralene film (4 μm), one half of core BH20 was imaged and analyzed using a Core Scanner (Avaatech, NL). The elements Al, Si, Ca, Ti, Mn, and Fe were scanned at 1 mA, 10 s, and with a tube voltage of 10 kV; Cu, Zn, Rb, Sr, and Zr were scanned at 2 mA, 20 s, and 30 kV. The core was scanned at a resolution of 2 mm, and the results are expressed as counts per second (cps).

Table 1
AMS ^{14}C dating results for core BH20.

Laboratory no.	Depth (cm)	Material	AMS ^{14}C age (yr BP)	Reservoir- corrected ^{14}C age (yr BP)*	Calibrated age (2σ, cal yr BP)	$\delta^{13}C$ (‰)
Beta - 571562	0.5	Bulk organic matter	920 ± 30	40 ± 30	34–72 (53)	−30.9
Beta - 571563	38.0	Bulk organic matter	1320 ± 30	440 ± 30	456–529 (502)	−28.2
Beta - 571564	78.5	Bulk organic matter	2440 ± 30	1560 ± 30	1377–1523 (1454)	−26.5
Beta - 571565	123.0	Bulk organic matter	2660 ± 30	1780 ± 30	1598–1679 (1656)	−28.4
Beta - 571566	160.5	Bulk organic matter	3220 ± 30	2440 ± 30	2357–2540 (2485)	−28.1
Beta - 571567	201.0	Bulk organic matter	3880 ± 30	3000 ± 30	3102–3254 (3189)	−28.1

* The reservoir age correction of 880 yr BP was used.

Pretreatment for grain-size analysis included immersing ~0.3 g subsamples in 10 mL 10% H_2O_2 and 0.5 mol/L HCl at ~200 °C to remove organic matter and carbonate, respectively. Deionized water was then added to the decarbonized samples and they were left to settle for 24 h. Next, $(Na_2PO_3)_6$ (10 mL, 10%) was added to each sample after siphoning off the supernatant, followed by ultrasonic dispersal for ~5 min. The samples were measured using a Mastersizer 2000 (Malvern, UK) laser grain-size analyzer (0.02–2000 μm), with 700 r/min agitator speed, 80 Hz ultrasonic intensity, and 1750 r/min pump speed. Each sample was measured three times to ensure repeatability. Forty-six samples were homogenized and analyzed by X-ray diffraction (XRD) using an X'PERT Pro MPD (PANalytical, NL).

The percentage water content was obtained by subtracting the weight of the freeze-dried subsamples from that of the wet subsamples. The weight LOI was measured at 1-cm intervals by combusting the samples in a muffle furnace. The weight loss after combustion at 550 °C represents the organic matter content, and that at 950 °C represents the carbonate content (Dean, 1974; Heiri et al., 2001). After subtracting the organic matter and carbonate contents the residue is regarded as silicate clastic material.

All pretreatments and geochemical experiments were conducted at the Key Laboratory of Western China's Environmental Systems (Ministry of Education), Lanzhou University, China.

3.2.3. Extraction, analysis, and proxy calculation of GDGTs

All freeze-dried and homogenized samples (~3 g) were ultrasonically agitated in a dichloromethane: methanol (v:v = 9:1) solution four times (15 min each) and then concentrated to dryness using N_2 gas. The total lipid extract was separated over a silica gel chromatography column using hexane, dichloromethane, and methanol as eluents to isolate the neutral and polar fractions (containing GDGTs), respectively (Chen et al., 2021). The polar fractions were redissolved and filtered through a 0.22 μm polytetrafluoroethylene (PTFE) filter prior to liquid chromatography–mass spectrometry (LC–MS) analysis. The GDGT analyses were performed using an Agilent 1290 series ultra-performance liquid chromatography–atmospheric pressure chemical ionization–6465B triple quadruple mass spectrometer (UPLC–APCI–MS/MS). The flow rate was 0.3 mL/min, an aliquot of 10 μL was injected and separated on two Hypersil Gold Silica columns in sequence (each 150 mm × 2.1 mm, 1.9 μm, Thermo Fisher Scientific; USA), maintained at 40 °C. The GDGTs were isocratically eluted with 84% A and 16% B for the first 5 min, where A = *n*-hexane and B = EtOA, followed by a linear gradient change to 82% A and 18% B from 5 to 65 min, and then a linear change to 100% B for 10 min to separate OH-GDGTs; elution with 100% B was continued for a further 5 min, before changing to 84% A and 16% B to equilibrate the pressure. Analyses were performed using the selective ion monitoring (SIM) mode to track *m/z* 1302, 1300, 1298, 1296, 1292, 1050, 1048, 1046, 1036, 1034, 1032, 1022, 1020, 1018, and 744 (C_{46}). All lipid extract analyses were conducted at the Key Laboratory of Western China's Environmental Systems (Ministry of Education), Lanzhou University, China.

The revised MBT (MBT′) and cyclisation of branched tetraether (CBT) indices of brGDGTs were calculated using [Eq. (1)] and [Eq. (4)] (see Table S1). The roman numerals denote the abundance of the corresponding brGDGT structures, and they refer to Weijers et al. (2007), Peterse et al. (2012), and Schouten et al. (2013). MBT'_{5ME} and $MBT_{5/6}$ were based solely on either 5- or 6-methyl brGDGTs (De Jonge et al., 2014; Ding et al., 2015) calculated using [Eq. (2)] and [Eq. (3)]. This is because Hopmans et al. (2016) improved the chromatographic procedure for analysis of brGDGTs and achieved the separation of 5- and 6-methyl brGDGTs in their studied sediments. The relative amounts of 6- vs. 5-methyl brGDGTs (defined as IR_{6ME}) were calculated according to De Jonge et al. (2015a) as [Eq. (5)]. The Branched and Isoprenoid Tetraether (BIT) index, based on the relative abundance of brGDGTs versus Crenarchaeol, was calculated using [Eq. (6)] (Hopmans et al., 2004).

4. Results

4.1. Lithology and chronology of core BH20

The sediments of core BH20 has a very low organic matter content, ranging from 7.32% to 16.25%, with an average of 13.35%, which is consistent with the water content that varied from 33.41% to 78.75%. The silicate content is substantially higher than the organic content, ranging from 79.39% to 90.75%, with the average of 82.89%. Core BH20 consists of lacustrine sediments with alternating thin (2–4 cm) grayish-white layers within the 48–84-cm depth range (Fig. 2a). These thin layers are characterized by rapid changes in lithology and they had an anomalously low water and organic matter content, and a high silicate content, and a relatively high sedimentation rate.

The chronology of core BH20 core is based six AMS ^{14}C dates after correction for an 880-year reservoir effect (Fig. 2b, c). The age model indicates that the base of the 218-cm-long core is ~3500 cal yr BP, giving an average sedimentation rate of ~0.63 mm/yr.

4.2. Variations in geochemical indices

The results of XRF scanning, grain-size, and LOI measurements are shown in Fig. 3. The variations in Al, Si, Ca, Ti, Zn, Rb, Sr, and Zr (in cps) are all positively correlated with each other for the entire core record (Table S2; Fig. S1). The application of principal component analysis (PCA) to the elements listed above showed that the first principal component (PC1) comprised 45% of the total variance, and it was more significant than components PC2 and PC3 (Table S3; Fig. S2).

The sediments of Lake Bihu are composed mainly of clay and silt, with a minor sand content (sand, silt and clay are here defined as the >64 μm, 4–64 μm, and < 4 μm fractions, respectively). The proportion of clay was the largest (average of 54.39%), followed by silt (average of 45.60%), and the average sand content was <1% (Fig. 3a). The median grain size (d (0.5)) in lake sediments ranges between 6.10 and 10.91 μm, with an average of 7.74 μm, whereas the mean of median grain size at soil sample from catchment and loess samples from the Ganjia Basin is 15 μm and 40 μm (Fig. 3b; Fig. 4a). The variations of the silt content, median grain size, and silicate content are generally consistent and they are well correlated ($p < 0.01$) (Fig. 3). The results of analyses of the composition and morphology of the minerals in samples from core BH20, analyzed by XRD and scanning electron microscopy (SEM), showed that the mineral composition is dominated by silicate minerals,

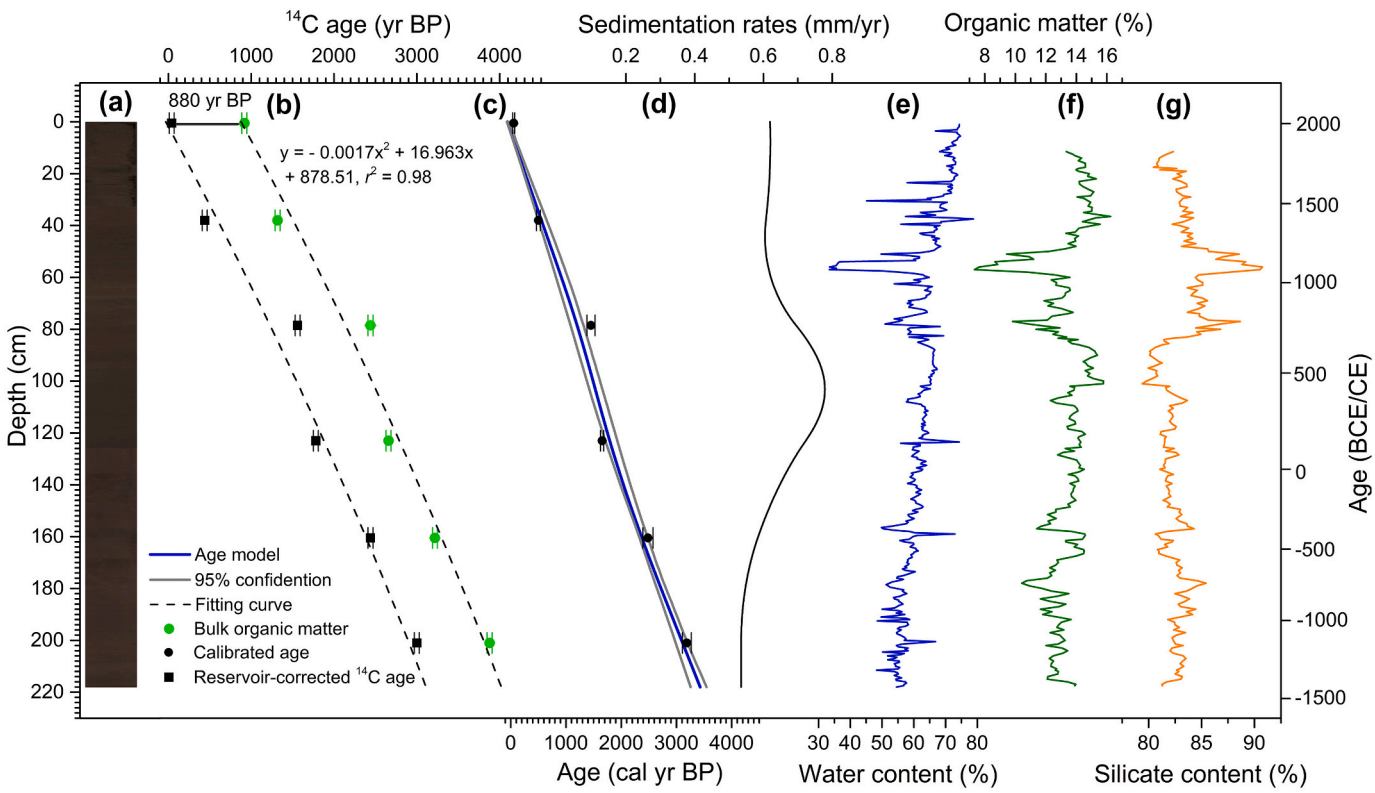

Fig. 2. Lithology and age model for core BH20. (a) Core photograph. (b) Calibration of the carbon reservoir effect (x and y represent depth and age, respectively). (c) Age–depth model. (d) Sedimentation rate. (e)–(g) High-resolution profiles of (e) water content, (f) organic matter content, (g) and silicate content, spanning the last 3500 years.

including quartz and aragonite, and that these minerals had not been transported over long distances (Fig. 4c–f).

4.3. Distribution of brGDGTs and paleotemperature reconstruction

4.3.1. Distribution of brGDGTs

Our results show that brGDGTs-Ia, IIa, IIa', IIIa', and IIIa were the most abundant compounds (total fractional abundance of 78.98%) in sediments of Lake Bihu. We found that these acyclic brGDGTs were also the dominant compounds in globally-distributed soils, including in China, and in lake surface sediments from East Africa (Fig. 5a). In contrast, the relative amounts of cyclopentane ring-containing brGDGTs in the sediment samples from Lake Bihu were generally lower, and sometimes not even detectable.

The pentamethylated (brGDGTs-II; 45.85%) and hexamethylated (brGDGTs-III; 27.42%) brGDGTs dominated the total brGDGTs in the Lake Bihu sediments, followed by tetramethylated (brGDGTs-I; 26.73%) brGDGTs. The isomer ratio (IR_{6ME}) varied from 0.26 to 0.38 (Table 2), revealing that the 5-methyl isomer brGDGTs, rather than 6-methyl material, are dominant in these sediments, which is in accord with values for Tibetan Plateau soils and with surface lake sediments from China and East Africa (Fig. 5b). However, the Lake Bihu sediments had much higher acyclic moieties, including Ia, IIa, IIIa, IIIa' and the pentamethylated brGDGTs were the most abundant. This differs from the distribution pattern for soils of the Tibetan Plateau and the surrounding areas within China, where IIc, IIIb' and IIIc brGDGTs were the most abundant (Fig. 5a, b). Ternary plots of the relative abundances of tetra-, penta-, and hexamethylated brGDGTs reveal that the global and Chinese soils have a tetramethylated dominance, whereas the Tibetan Plateau soils have a greater proportion of pentamethylated brGDGTs, which is also the case for both Chinese lakes and Lake Bihu (Fig. 5b). Notably, the surface lake sediments from the Tibetan Plateau have a different distribution pattern to that of the plateau soils, whereas the Lake Bihu sediments have a same distribution pattern to these soils, which indicates that the distribution of brGDGTs in the lake surface sediments can be regulated by the input of soils, and this distribution pattern is also manifested on a global basis.

4.3.2. BrGDGT calibrations for paleotemperature reconstruction

The MBT′, MBT'_{5ME}, $MBT_{5/6}$, and IR_{6ME} indices in core BH20 vary consistently with each other (Fig. S4), and the absolute mean values were also similar, ranging from 0.27 to 0.41 (Table 2). These indices fluctuated with large amplitudes on multidecadal to centennial timescales during the late Holocene. In contrast, the CBT shows the opposite trend to all the other indices throughout the entire sedimentary sequence, with an absolute mean value of 0.45.

Previously published brGDGT calibrations for modern temperature reconstruction based on global (De Jonge et al., 2014) and Tibetan Plateau (Ding et al., 2015) soils, and surface lake sediments from East Africa (Russell et al., 2018), China (Dang et al., 2018), and the Tibetan Plateau (Günther et al., 2014) were applied to our lake sediment dataset (Table S4; Fig. S3). The brGDGTs-based temperature variations at Lake Bihu area during the past 3500 years were reconstructed using the transfer functions based on the modern datasets mentioned above (Table S4). The temperatures reconstructed from these transfer functions are strongly correlated with the brGDGT indices (MBT′, MBT'_{5ME}, $MBT_{5/6}$, and IR_{6ME}), except for the reconstruction using transfer functions based on surface lake sediments of the Tibetan Plateau, which shows the opposite trend during the last 3500 years (Fig. S4). Notably, the reconstructed temperature record based on Günther et al. (2014) for the surface lake sediments of the Tibetan Plateau ranged from 0.70 to 3.98 °C, with an average of 2.19 °C (Table 2).

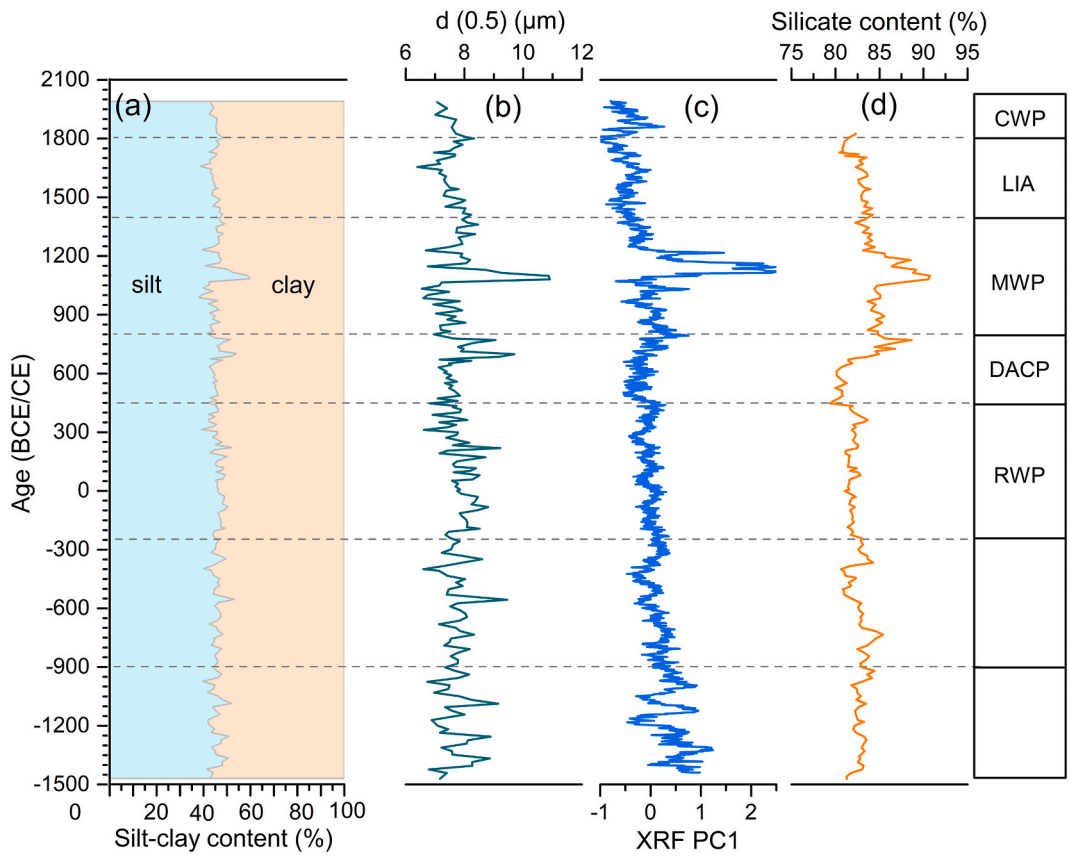

Fig. 3. Summary of the grain size and geochemical results for core BH20. (a) Percentages of clay and silt. (b) Median grain size. (c) Sample scores on PC1 of the elements determined by XRF scanning. (d) Silicate content. The sequence during the last 3500 years is divided into the following intervals: 1500–900 BCE, 900–250 BCE, Roman Warm Period (RWP, 250 BCE–450 CE), Dark Ages Cold Period (DACP, 450–800 CE), Medieval Warm Period (MWP, 850–1400 CE), Little Ice Age (LIA, 1400–1800 CE), and Current Warm Period (CWP, 1850 CE–present).

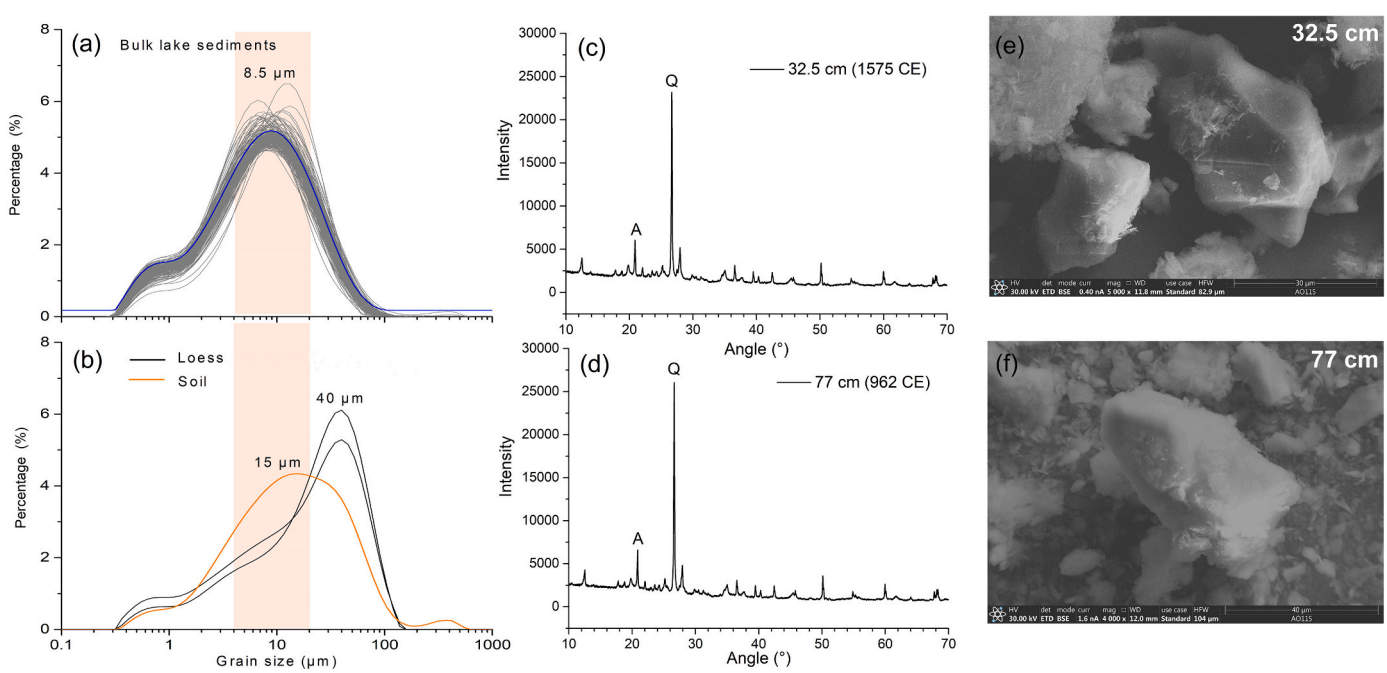

Fig. 4. Establishment of a precipitation proxy for the sediments of Lake Bihu. (a) Measured grain-size distributions of 216 samples from core BH20. (b) Measured grain-size distributions of samples of the surrounding soils and loess deposits. (c)–(f) Mineral species and morphology of the lacustrine sediments of core BH20, determined by SEM and XRD analysis of representative samples from different depths. A = aragonite, Q = quartz.

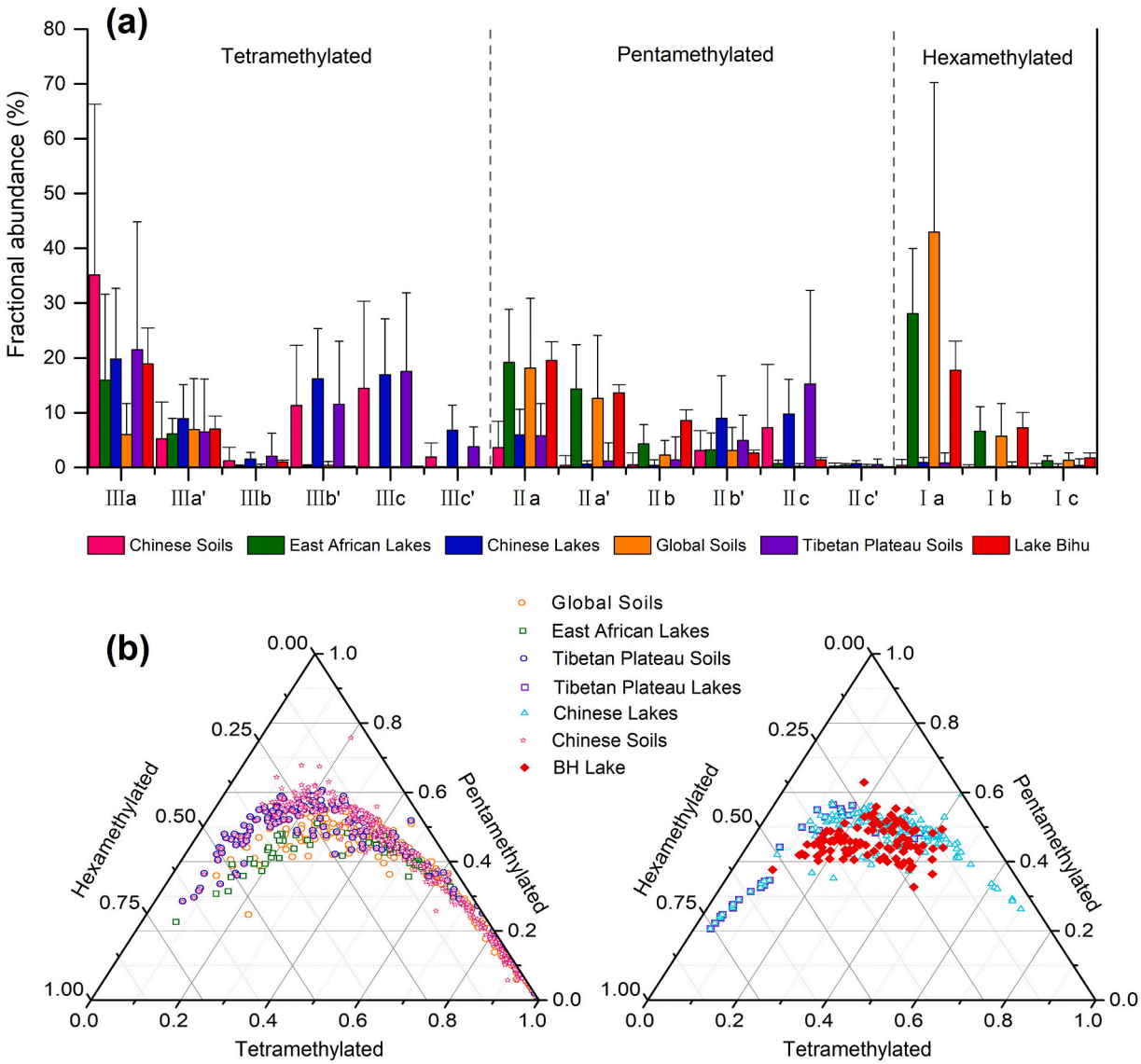

Fig. 5. Comparison of the fractional abundances of brGDGTs in the sediments of Lake Bihu with previously published data. (a) Comparison of the fractional abundances of individual brGDGTs in Lake Bihu sediments with previously published data, including global soils (De Jonge et al., 2014); the Tibetan Plateau and soils within the China (Günther et al., 2014; Ding et al., 2015; Naafs et al., 2017; Li et al., 2018; Zang et al., 2018; Wang et al., 2018, 2019; Ning et al., 2019; Pei et al., 2019; Qian et al., 2019; Dearing Crampton-Flood et al., 2020; Cao et al., 2020; Zhao et al., 2020; Wang and Liu, 2021; Wang et al., 2020, 2023); and surface lake sediments from the Tibetan Plateau (Günther et al., 2014), lakes within China (Dang et al., 2018; Ning et al., 2019; Yao et al., 2019; Qian et al., 2019; Cao et al., 2020; Zhao et al., 2020; Wu et al., 2021; Wang et al., 2023), and East African lakes (Russell et al., 2018). (b) Fractional abundances of summed tetra-, penta-, and hexamethylated brGDGTs in the sediments of Lake Bihu and the previously published dataset shown in (a).

Table 2
brGDGTs indices and temperature reconstruction based on soil and surface lake sediment calibrations.

	MBT′	MBT′$_{5ME}$	MBT$_{5/6}$	CBT	IR$_{6ME}$	MAF (Günther et al., 2014)	MAF (Dang et al., 2018)	MAF (Russell et al., 2018)	MAF (Ding et al., 2015)	MAF (De Jonge et al., 2014)
Maximum	0.46	0.55	0.63	0.66	0.38	3.98	16.29	16.77	11.30	8.87
Minimum	0.09	0.13	0.20	0.28	0.26	0.70	11.96	2.86	−2.3	−4.62
Mean	0.27	0.35	0.41	0.45	0.32	2.19	14.19	10.23	4.47	2.53

5. Discussion

5.1. Temperature change on the northeastern Tibetan Plateau during the last 3500 years

5.1.1. brGDGTs-induced temperature variations in Lake Bihu

The correlation of brGDGTs (MBT and CBT indices) with air temperature and soil pH was initially identified in global soil datasets by Weijers et al. (2007). Subsequently, in the last decade, it was found that brGDGTs in different geological archives, including lake sediments (Günther et al., 2014; Dang et al., 2018; Zhang et al., 2022a), peats (Naafs et al., 2017), and marine sediments (De Jonge et al., 2015b) are correlated with water/air temperature. In lake systems, the brGDGTs in the lake sedimentary pool has mixed sources, because brGDGTs are

abundant in soils and thus soil inputs can undoubtedly affect brGDGT distributions in lake sediments. However, a recent study found a strong similarity between brGDGT fractional abundances (MBT'/MBT'_{5ME}) and temperature, across almost all sample types examined (based on a global dataset, including soils, peats, groundwater, bone, and suspended/settling particulate matter in lacustrine, riverine, and marine settings) (Raberg et al., 2022). This wide distribution of brGDGTs indicates that there is no vector bias for bacterial communities in the natural environment, which is supported by published data from surface lake sediments and soils on the Tibetan Plateau and elsewhere within China (Fig. S5). The MBT′ is significantly correlated with MAAT and MAF, both in surface soils and lake sediments, and especially in surface lake sediments from China and has the lowest degree of dispersion, although the distribution of brGDGTs in lake sediments may contain a soil-derived signal. In addition, we used the BIT index, which is an index of lipid biomarkers correlated with the fluvial input of terrestrial organic material, to assess the stability of the soils-derived brGDGTs in the lake system (Hopmans et al., 2004). A survey of globally distributed marine and lacustrine surface sediments shows that the BIT index in these environments is correlated with the fluvial input of terrestrial organic material, and the BIT index shows high values in marine and lake environments with large fluvial inputs (Hopmans et al., 2004). Indeed, previous studies showed that high values of the BIT index in Holocene lake sediments from Lake Cuoqia (China), Lake Paloma (Chili), Lake Siso (Spain) and Lake Bihu—spanning a large environmental gradient (Hopmans et al., 2004; Zhang et al., 2022a)—indicate a stable microbial community and the supply of terrigenous brGDGTs to these lacustrine environment (Sinninghe Damsté et al., 2009). Consequently, this thermometer can reasonably be used for paleotemperature reconstruction, given that the distribution of brGDGTs is significantly associated with the atmospheric temperature, whether in lakes or the surrounding soils.

These extensive modern sample datasets have been widely used in recent decades to produce calibration equations based on multiple linear regression analysis (see details in Section 4.3.2). However, there is a warm-season bias of brGDGT-based temperature reconstructions when using these calibration equations, which is caused by the freezing of lake water at high elevations and latitudes during the cold season, as reported in previous studies (Shanahan et al., 2013; Deng et al., 2016; Hu et al., 2016; Cao et al., 2020; Zhang et al., 2021, 2022a). As a high-altitude water body, Lake Bihu (4360 m a.s.l.) may freeze during the cold season, likely insulating the lake water from changes in air temperature and maintaining a relatively stable water temperature above 0 °C when the air temperature is below 0 °C. Thus, the water temperature of Lake Bihu mainly records changes in air temperature during the ice-free season (e.g., MAF, between May and October) inferred from the nearest meteorological station (Linxia) data, after elevation correction. Additionally, lacustrine sediments were recently shown to correlate with the MAF warm-season air temperature index, on a global scale (Martínez-Sosa et al., 2021; Raberg et al., 2021). The seasonal bias of temperature reconstructions indicates that there are systematic changes in the length of the warm season, as well as the seasonal period of brGDGTs production by different microbial communities, which can result in the overestimation of brGDGTs-based temperatures (Shanahan et al., 2013; Deng et al., 2016; Dang et al., 2018; Zhang et al., 2022a).

Given the warm-season temperature bias, we used all the brGDGTs-temperature calibrations to reconstruct MAF changes of the surface sediments from core BH20, which were then compared, after elevation calibration, with instrumental data for the period 1951–2020 (Table S4). The results indicate that the brGDGTs-inferred MAF reconstructed from Günther et al. (2014) (3.09 ± 1.10 °C) matches well with the instrumental MAF (3.01 °C), but it is markedly higher than the instrumental MAAT (−5.72 °C). This suggests that the MAF reconstructed using the brGDGTs transfer equation of Günther et al. (2014) from the surface sediments of core BH20 (and with the deeper sediments) is reliable, and that the amplitude of MAF variability is more reasonable than those obtained using other transfer equations (some of which produced the absolute value of 16 °C; Fig. S4). We conclude that careful selection of an appropriate calibration equation is needed to screen the brGDGTs-based temperature dataset. For example, the equation based on the group of lakes from East Africa produced results that often ranged from 1.6 to 26.8 °C (Russell et al., 2018), while for the Tibetan Plateau, an alpine region, the range of temperature variation was from −1.5 to 3.6 °C (Günther et al., 2014), which is consistent with that of observations from Dalijia Mountain. Moreover, the modern temperature estimated from surface sediment brGDGTs is supported by a comparison with the measured temperature, which further validates the applicability of this equation. There are similar cases in which brGDGTs calibrations using linear regression of measured temperature and brGDGTs-based proxies (MBT/MBT′, CBT) from Bangong Co (Wang et al., 2016b, 2021), Linggo Co (He et al., 2020) and Aweng Co (Li et al., 2017), together with those of Günther et al. (2014), are applicable to Tibetan Plateau lakes, although these brGDGTs-inferred MAAT records may be biased towards the most biologically productive season.

Regarding the overall trend, the regional MAF reconstruction based on surface lake sediments from the Tibetan Plateau shows pronounced fluctuations on decadal to centennial timescales during the warm periods of 1500–900 BCE, and the MWP and CWP, and a distinct cooling trend during 900–250 BCE and the LIA (Fig. 6a). The absolute values of the reconstructed temperatures range between 0.70 and 3.98 °C, with an average of 2.19 °C over the past ~3500 years. Our record shows that the regional MAF during the MWP optimum exceeded the MAF during the CWP. Additionally, the reconstructed MAF increased from the beginning of the 20th century across the NETP, which is consistent with the positive temperature trend shown in local instrumental observations, and in the results of climate modeling and analysis (Chen et al., 2015a; Yao et al., 2019; You et al., 2021). However, it should be noted that the sampling resolution during the RWP is relatively low.

5.1.2. Paleotemperature variations on the northeastern Tibetan Plateau and in the surrounding regions

We reviewed various published late Holocene quantitative temperature records to characterize the pattern of temperature changes on the NETP and in the surrounding regions (although there are a limited number of high-resolution quantitative temperature records for this region) (Yang et al., 2003; Liu et al., 2006; Liu et al., 2009; Wu et al., 2013; He et al., 2013b; Zhao et al., 2013; Feng et al., 2019, 2022). Comparison of the late Holocene NETP temperature records indicates that warm intervals can be correlated to the WCP, MWP, RWP, and the interval of 1500–900 BCE; while cold intervals can be correlated to the LIA, DACP, and the interval of 900–2500 BCE (Fig. 6). Specifically, the MAAT reconstructed from tree-ring widths from the central-eastern Tibetan Plateau indicates distinct warm intervals during the RWP (403–413 CE), with a temperature 2.89 °C higher than that of the mean for 1970–2000 CE, and during the MWP (864–882 and 965–994 CE), when the temperature was 2.81 °C higher. Cold intervals are indicated during the DACP (686–705 CE), with a cooling of ~1.71 °C, and during the LIA (1599–1702 CE), with a cooling of ~1.77 °C (Liu et al., 2009). Likewise, synthetic data reflecting paleotemperature changes from the NETP show distinct climatic episodes, with warm intervals during 800–1100 and 1150–1400 CE, a cold interval during the LIA between 1400 and 1900 CE, and an earlier cold period between the 4th and 6th centuries (Yang et al., 2003). We also compared the existing lacustrine sedimentary records with our reconstruction and found that the brGDGTs-inferred MAF from Lake Cuoqia (Zhang et al., 2022a) and MAAT from Lake Lugu (Zhao et al., 2021) and Lake Tiancai (Feng et al., 2019, 2022), on the southwestern Tibetan Plateau, are consistent, although these records have a greater temperature variability and more pronounced centennial-scale fluctuations. Likewise, alkenone-inferred summer/warm-season temperature records from Lake Qinghai (Liu et al., 2006; Hou et al., 2016), Lake Sugan and Lake Gahai (He et al., 2013b) on the northeastern Tibetan Plateau, and summer temperatures inferred from subfossil chironomids from Lake Heihai (Chang et al.,

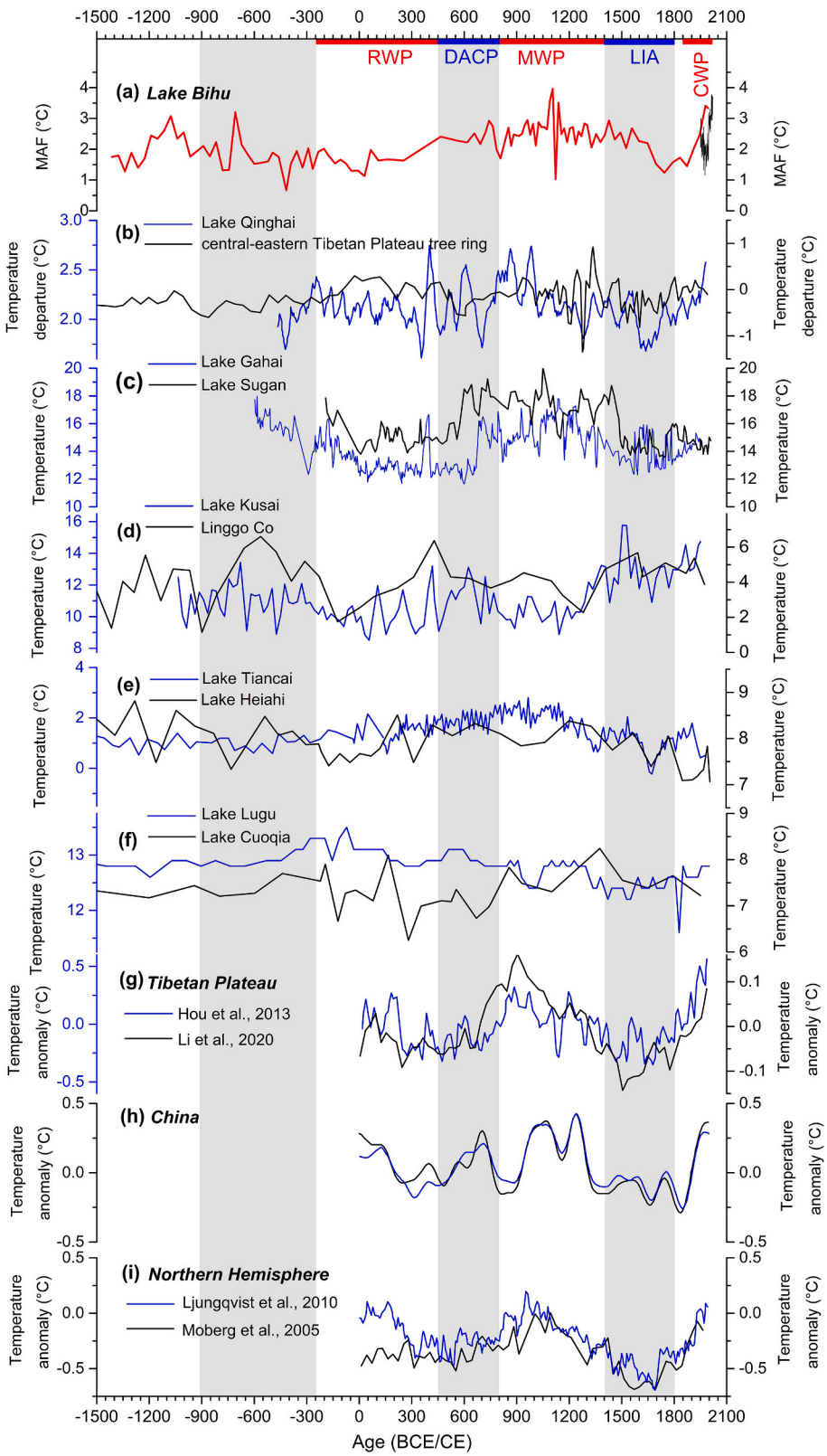

Fig. 6. Comparison of the reconstructed temperature variations at Lake Bihu and other paleotemperature records from the Tibetan Plateau, China, and the Northern Hemisphere during the last 3500 years. (a) brGDGTs-based MAF at Lake Bihu (black line shows instrumental MAF values during 1951–2020 CE) (this study). (b) Alkenone-based temperature record from Lake Qinghai (Liu et al., 2006) and reconstructed annual mean temperatures based on tree-ring width from the central-eastern Tibetan Plateau (Liu et al., 2009). (c) Alkenone-based temperature record from Lake Sugan and Lake Gahai (He et al., 2013b). (d) brGDGTs-inferred MAAT records from Lake Kusai (Wu et al., 2013) and Linggo Co (He et al., 2020); (e) brGDGTs-inferred MAAT record from Lake Tiancai (Feng et al., 2019, 2022), and mean July temperatures inferred from subfossil chironomids from Lake Heihai (Chang et al., 2017). (f) brGDGTs-inferred MAAT record from Lake Lugu (Zhao et al., 2021) and brGDGTs-inferred MAF record from Lake Cuoqia (Zhang et al., 2022a). (g) Composite temperature record for the entire Tibetan Plateau (Hou et al., 2013; Li et al., 2020). (h) Ensemble temperature reconstructions for China based on principal component regression (red lines) and partial least squares (blue lines) methods on the centennial timescale (with 5-point smoothing using a Fast Fourier Transform filter) (Ge et al., 2013). (i) Composite temperature anomalies for the Northern Hemisphere (Moberg et al., 2005; Ljungqvist, 2010). The gray shaded vertical bars indicate cold periods. (For interpretation of the references to colour in this figure legend, the reader is referred to the web version of this article.)

2017) on the southeastern Tibetan Plateau, are also consistent with our record. However, some of the temperature records are not well correlated with our MAF record, including the brGDGTs-inferred MAAT reconstructions from Lake Kusai (Wu et al., 2013) on the northeastern Tibetan Plateau, and from Linggo Co (He et al., 2020) on the central Tibetan Plateau, and Bangong Co (Wang et al., 2021) and Aweng Co (Li et al., 2017), on the western Tibetan Plateau. We hypothesize that factors like seasonal biases of the proxies, age-model inaccuracies, and strong regional contrasts (including differences in altitude and topography, and lake size and depth, and vegetation cover and associated climate feedbacks) may affect the consistency of these records.

We also compared the temperature records from the NETP and

nearby regions (Liu et al., 2007; Zhu et al., 2008; Li et al., 2020, 2022a and therein; Fig. 6b–g) with records from other regions in China (Yang et al., 2002; Ge et al., 2010, 2013; Fig. 6h) and the Northern Hemisphere (Moberg et al., 2005; Mann et al., 2009; Ljungqvist, 2010; Fig. 6i). This shows that temperature fluctuation during the last 3500 years were generally consistent on the centennial timescale. In addition, our reconstruction from Lake Bihu shows a significant warming trend after the 1900s, which is consistent with modern observations that show that the rate of modern warming of the Tibetan Plateau is twice that of the global average (Chen et al., 2015a), indicating an amplified response of air temperature variations on the Tibetan Plateau (Pepin et al., 2015).

5.2. Hydroclimatic changes on the northeastern Tibetan Plateau during the last 3500 years

5.2.1. Hydroclimatic changes at Lake Bihu

Previous studies have shown that detrital elements (including Al, Si, Ti) can be used to reflect the erosional energy in lake catchments, which is closely linked to the intensity of runoff or precipitation within the catchment (Yancheva et al., 2007; Kylander et al., 2011; Jin et al., 2015). Specifically, higher sedimentary contents of these detrital contents indicate more intense catchment erosion in response to increased regional precipitation (Shen et al., 2013; Zhang et al., 2017; Peng et al., 2019). Additionally, we used the BIT index to eliminate a possible aeolian source in the Lake Bihu sediments. The generally high and stable BIT values throughout the core (Fig. S6) demonstrate the consistency of the level of terrigenous erosion, reflecting a stabile precipitation regime, and corresponding to the geochemical index (Fig. 7a). The high-resolution record of sample scores on PC1, based on the XRF-scanning elements, offers the possibility of directly linking the lake sedimentary record with erosion within the catchment.

The grain-size distributions of lake sediments can reflect the transport dynamics and sedimentary environment (Peng et al., 2005; Liu et al., 2016; Zhang et al., 2017): coarse-grained particles may reflect either strong winds associated with aeolian transport (An et al., 2012; Qiang et al., 2014; Li et al., 2022b), or heavy precipitation-induced runoff input and alluvial deposition (Chen et al., 2003; Zhang et al., 2003a; Liu et al., 2016). A polymodal grain-size distribution of lake sediments can be caused by various factors, including the source of the clastic material, specific depositional processes and environments, lake size and shape, lake level fluctuations, and the hydrological dynamics of the lake water (Sun et al., 2002; Xiao et al., 2013; Liu et al., 2016). The grain size of the loess samples we collected from the Ganjia Basin is larger than that of sediments and soils of the Lake Bihu catchment, which indicates that the loess deposits are unlikely to be wind-transported to the catchment, and thus we can exclude an aeolian transport mechanism for the lake sediments (Fig. 4b). The lithology of the Lake Bihu sediments changed only slightly during the late Holocene,

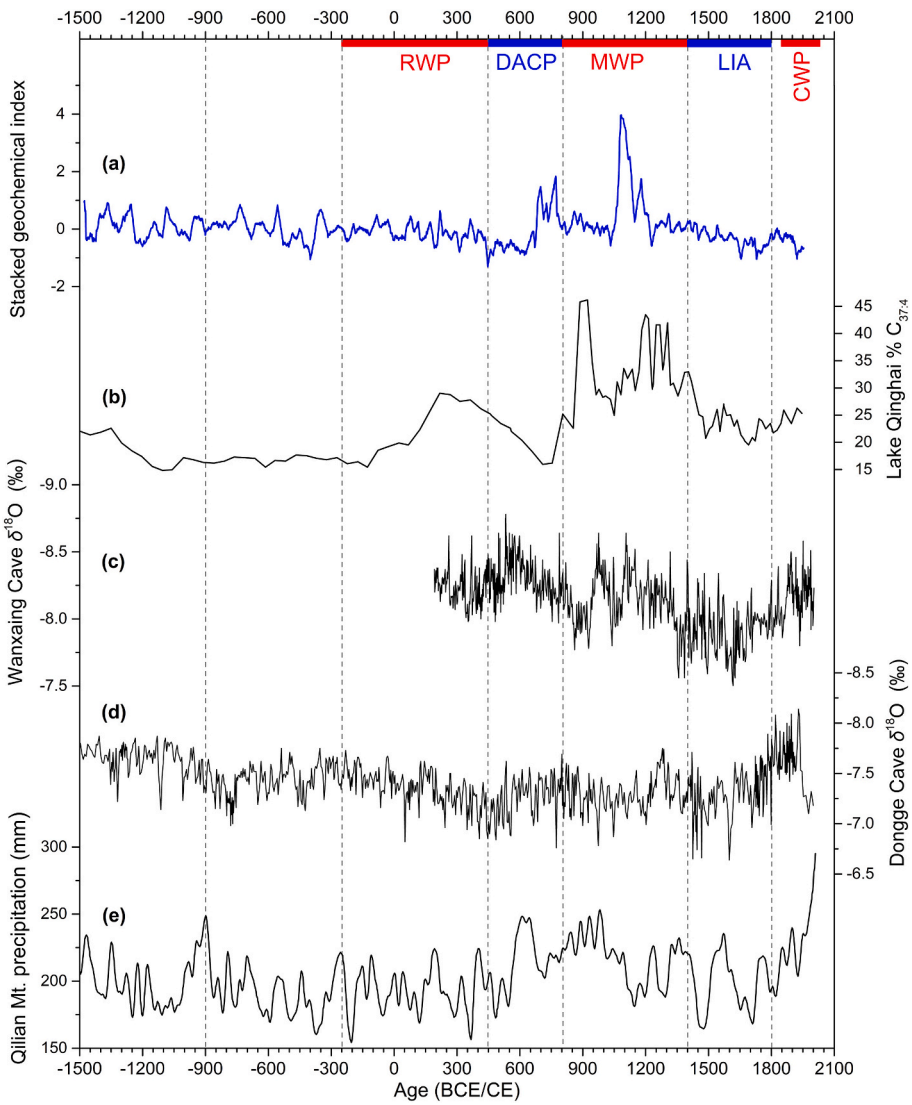

Fig. 7. Comparison of reconstructed precipitation on the northeastern Tibetan Plateau with that in the EASM region during the last 3500 years. (a) Reconstructed precipitation inferred from normalized stacked proxy indicators of the sediments of Lake Bihu. The normalized stacked values are calculated as: $(x_i - \bar{x}) / \sigma$ (where $\bar{x}$ is the mean and σ is the standard deviation). (b) Alkenone-inferred salinity record from Lake Qinghai (Liu et al., 2006). (c)–(d) Stalagmite $\delta^{18}O$ records from Wanxiang Cave (Zhang et al., 2008) and Dongge Cave (Wang et al., 2005). (e) Estimates of annual precipitation on the northeastern Tibetan Plateau based on an absolutely dated tree-ring chronology with 50-year smoothing (Yang et al., 2014). The locations of the sites are shown in Fig. 1a.

being dominated by deep-water lake facies, and thus any variations of the grain-size parameters are not associated with changes in the sedimentary environment. Lake Bihu is small, semi-open, and relatively shallow, and the water is primarily supplied by runoff during the rainy summers; also, the catchment is narrow and the detrital materials are transported only a limited distance (Fig. 4e–4f). Moreover, Lake Bihu is unlikely to be affected by sediment remobilization caused by lake-level fluctuations, and thus the grain size record likely reflects changes in runoff-supplied clastics driven by precipitation variations. Clastic materials in the catchment area are eroded and transferred to the lake via runoff; coarse particles are mainly deposited near the lake shore, while fine particles are transported to the deep water, where the site of core BH20 is located (Fig. 4b). Thus, we consider the grain size of the Holocene sediments in Lake Bihu is an indicator of precipitation-driven runoff from the steep slopes of the catchment, and an increased proportion of fine silt reflects a decrease in precipitation, and that an increased proportion of coarse silt reflects an increase in precipitation. The variation of the median grain size is consistent with that of silt fraction (which dominates the sediments) and it reflects the overall changes in the grain-size composition. The median grain size, sample scores on PC1 of the XRF-scanned elements, and the silicate content estimated from the LOI vary consistently on decadal to centennial timescales (Fig. 3). We produced a normalized index based on the stacking of these geochemical indices, to eliminate any errors associated with individual proxies (Fig. 7a). We interpret this index as an indicator of runoff variations, controlled by the summer monsoon precipitation in the EASM region, since the summer monsoon precipitation comprises up to 85% of total annual precipitation.

As shown in Fig. 7, the results reveal several distinct decadal- to centennial-scale climatic events, including the wet periods of 1500–900 BCE, RWP, MWP, and CWP, and the dry periods of 900 BCE–250 CE, DACP, and LIA. Additionally, SEM analysis showed that the degree of roundness of quartz grains during the MWP was higher than that during the LIA (Fig. 4), indicating stronger transport and depositional dynamics during the MWP, which can be attributed to increased runoff or precipitation within the catchment. Precipitation during the MWP was the highest during the past 3500 years, and it was also high during the CWP, with a peak at ~1850 CE, after which it decreased slightly. However, precipitation was overall relatively stable, except for brief events at the end of the DACP and in the middle of the MWP. We suggest that several factors may have affected the hydrology of the lake catchment, as follows. 1) Lake Bihu, as an alpine lake, is an ideal hydrometer because the lake water is mainly fed directly by atmospheric precipitation during the summer; thus, hydrological records from such lakes can reliably represent precipitation changes. For example, alpine Lake Daye, in the Qinling Mountains, is characterized by synchronous changes in lake level and atmospheric precipitation (Chen et al., 2021), and this may be one of the reasons for the relatively stable hydrological fluctuations within such small alpine lakes. 2) Soil erosion induced by precipitation is a major driver of the influx of clastic sediments, and thus the geochemical indicators can sensitively reflect changes in precipitation. 3) The hydrology of lake catchments is also influenced by the vegetation conditions (Li et al., 2022b). The vegetation around Lake Bihu is dominated by alpine meadow and the vegetation coverage is high during the warm and wet season, thus maintaining stable hydrological conditions and reducing runoff and soil erosion in the catchment.

5.2.2. Hydroclimatic variations across the NETP and EASM region

We used a stacked proxy record based on the geochemical indices from Lake Bihu to reconstruct the hydrological and climatic history of the NETP over the last ~3500 years, which we compared with typical hydrological records from the EASM region (Fig. 7). Several studies have reported stalagmite $\delta^{18}O$ data from the middle to late Holocene for the EASM region, and they are widely interpreted as a proxy for summer monsoon intensity, with lower $\delta^{18}O$ values representing a strong Asian summer monsoon, and vice versa (Wang et al., 2005; Zhang et al., 2008). For example, $\delta^{18}O$ records from Wanxiang Cave, located at the junction of the Tibetan Plateau and Chinese Loess Plateau, ~300 km from Lake Bihu, showed pronounced $\delta^{18}O$ enrichment during the DACP and LIA, compared with the RWP, MWP, and CWP, suggesting decreased Asian summer monsoon precipitation during the DACP and LIA (Zhang et al., 2008; Fig. 7c). Stalagmite records from Dongge Cave in southern China also show strongly enriched $\delta^{18}O$ values during the 900–250 BCE and the DACP, and LIA periods, compared to those during 1500–900 BCE, and the MWP and CWP, indicating decreased and increased Asian summer monsoon precipitation, respectively (Wang et al., 2005; Fig. 7d). Additionally, stalagmite $\delta^{18}O$ records from Huangye Cave (Tan et al., 2011) and Sahiya Cave (Sinha et al., 2015), on the Tibetan Plateau, also show temporal variations like those of the stacked proxy record from core BH20. Overall, these stalagmite $\delta^{18}O$ records and the precipitation reconstruction from Lake Bihu show almost parallel temporal changes.

The hydroclimatic patterns reconstructed from Lake Bihu during the last 3500 years are supported by precise tree-ring records from the adjacent regions of the NETP, where precipitation is controlled by the EASM (Yang et al., 2014). A high-resolution tree-ring based record from Dulan on the NETP indicates that the MWP was accompanied by pronounced wet springs during the period 929–1031 CE, with the peak occurring at ~974 CE (Zhang et al., 2003b). Furthermore, a tree-ring record of annual precipitation from the Qilian Mountains of the NETP suggests dry periods during the 4th century BCE and the second half of the 15th century CE; the driest individual year (since 1500 BCE) was 1048 BCE, while the wettest year was 2010 CE (Yang et al., 2014; Fig. 7e). Similarly, a tree-ring record from the NETP, reflecting moisture conditions at the onset of the growing season, shows two prominent low-growth periods corresponding to drought events centered on 1480 and 1710 CE, while notable high-growth periods were centered on 590 and 1570 CE, as well as in the last 30 years (Shao et al., 2010).

Hydroclimatic changes inferred from high-resolution lacustrine sedimentary records across the NETP and EASM region also co-vary on multidecadal to centennial timescales. For example, long-term trends in precipitation/salinity at Lake Qinghai, inferred from sedimentary C/N ratios, grain-size (Xu et al., 2015), and $\%C_{37:4}$ of alkenones (Liu et al., 2006; Fig. 7b) are like those of the precipitation reconstructions from the sediments at Lake Gonghai (Liu et al., 2011a) and Lake Dali (Xiao et al., 2008), in northern China. In summary, the existing high-resolution, well-dated climate proxy records, representing Asian summer monsoon precipitation, suggest that the hydroclimate varied synchronously across the NETP and EASM region during the last 3500 years, on multidecadal to centennial timescales. Overall, wet hydroclimatic conditions occurred during warm periods and relatively dry conditions during cold periods.

5.3. Driving mechanisms of late Holocene climatic variations on the NETP

Possible forcing mechanisms of the distinct warm–wet and cold–dry climatic patterns over the NETP and northern China during the last 3500 years include solar irradiance, volcanic eruptions, greenhouse gases, and atmospheric–oceanic modes (e.g., El Niño–Southern Oscillation (ENSO, closely linked to variations in equatorial sea surface temperature (SST)), and the Intertropical Convergence Zone (ITCZ), and Western Pacific Subtropical High (WPSH)). Next, we evaluate these possible factors.

The quantitative MAF reconstruction from Lake Bihu and total solar irradiance are highly correlated on decadal and centennial timescales, suggesting that larger-scale temperature variability (Steinhilber et al., 2012; Fig. 8a and c) may arise from direct heating of the NETP, mainly during the summer months, although evidence for this is lacking on the inter-annual timescale. In addition, the abrupt temperature rise during the CWP was likely caused by the increase in greenhouse gases during the industrial period (post-1850 CE) (Crowley, 2000; Fig. 8h), as noted in numerous other climate studies (IPCC, 2021). It is also well known

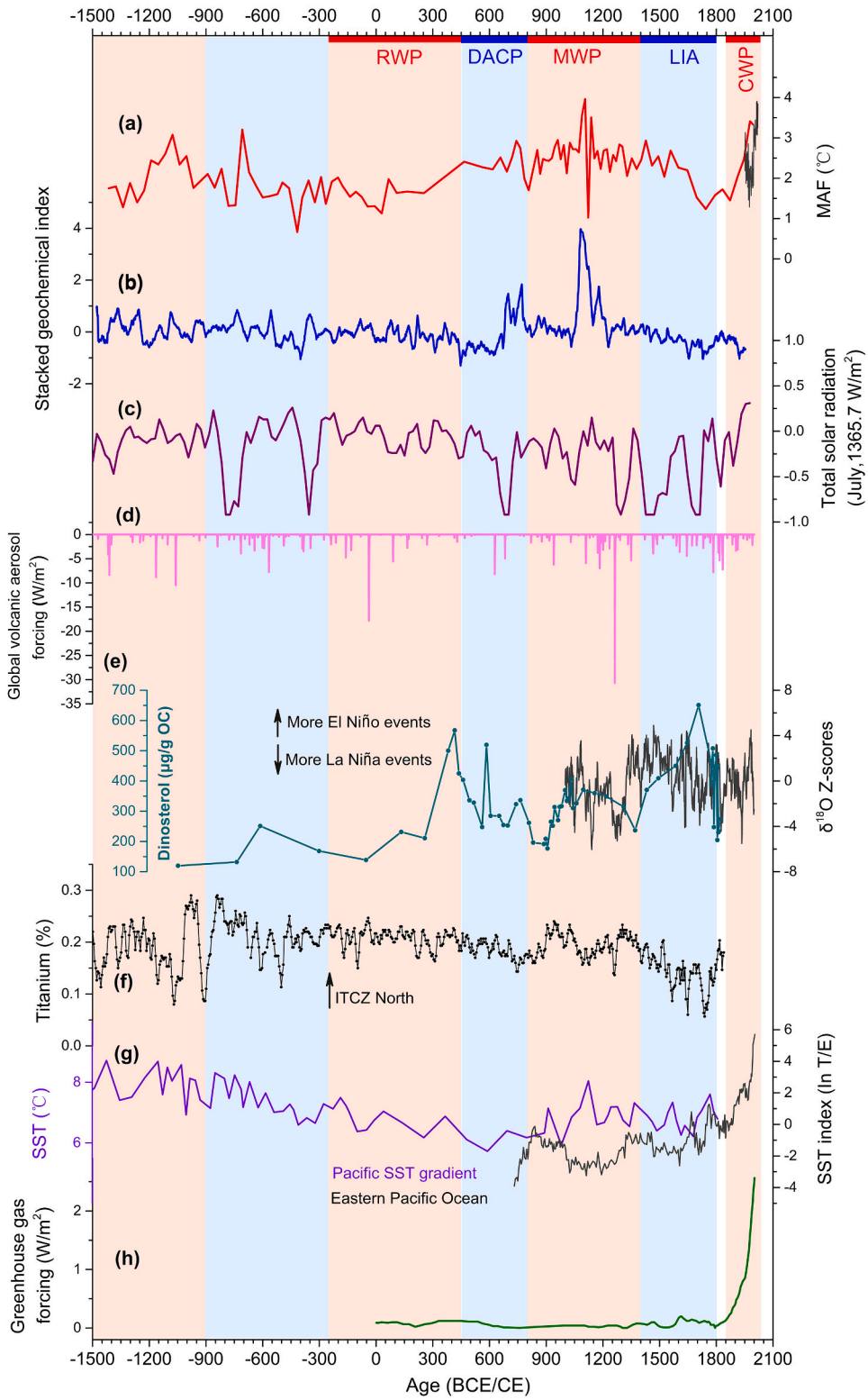

Fig. 8. Possible forcing mechanisms of climate change on the Tibetan Plateau during the past 3500 years. (a) Reconstructed precipitation basing on the stacked geochemical index, and (b) brGDGTs-based MAF (gray line showing instrumental MAF values during 1951–2020 CE) for Lake Bihu (this study). (c) Reconstructed total solar irradiance (Steinhilber et al., 2012). (d) Global volcanic aerosol forcing (Sigl et al., 2015). (e) Dinosterol abundance (a molecular organic geochemical proxy) in ODP Hole 1228D on the Peru margin, indicating El Niño activity (dark cyan; Makou et al., 2010), and composite stalagmite $\delta^{18}O$ record from the Asian–Australian monsoon region (gray; Zhang et al., 2022c). (f) Ti concentration in the sediments of the Cariaco Basin (Haug et al., 2001). (g) Zonal SST gradient for the tropical Pacific calculated as the difference between the western (Stott et al., 2004) and eastern (Rein et al., 2005) Pacific Ocean (violet line), and SST reconstruction from El Junco in the eastern Pacific Ocean (gray line; Conroy et al., 2009). (h) Greenhouse gas forcing (Crowley, 2000). The light brown shaded columns indicate warm–wet periods, and the blue shaded columns indicate cold–dry periods. (For interpretation of the references to colour in this figure legend, the reader is referred to the web version of this article.)

that hemispheric to global climatic cooling following strong or continuous volcanic eruptions may last decades, enabling the multi-centennial to millennial quantification of the climate response to volcanic forcing (Castellano et al., 2005; Sigl et al., 2015; Toohey et al., 2016). A reconstruction of global volcanic aerosol forcing suggests that there were more eruptions during the DACP and LIA, and fewer eruptions during the MWP; these eruptions can potentially be linked to several of the extreme cold events in our reconstruction (Sigl et al., 2015; Fig. 8d). It should be noted that accurately-dated tree-ring records are well-suited to resolving the climatic response to volcanic eruptions which often show close relationships with climate variables (Mann et al., 2012; Sigl et al., 2015). The coldest decade in the past 3500 years, indicated by the greatest reduction in tree growth during a sustained cooling period, was associated with several successive volcanic eruptions over the Tibetan

Plateau and surrounding regions (Briffa et al., 2013; Salzer et al., 2014; Zhang et al., 2014).

In addition to temperature records, precipitation variations during the late Holocene, reconstructed from the numerous proxy indices obtained from the NETP and the wider EASM region, are also potentially related to external forcing, namely solar activity on decadal to millennial timescales (Wang et al., 2005; Zhang et al., 2008; He et al., 2013a; Li et al., 2022b; Liu et al., 2022). Increased summer precipitation over these regions was driven by higher solar irradiance, corresponding to a greater thermal gradient between the East Asian continent and the northern Pacific Ocean, and thus a northward migration of the WPSH (Liu et al., 2011b; Chen et al., 2015b; Shi et al., 2018; Shi and Wang, 2019); and there was also a northward shift of the ITCZ during warm periods (Haug et al., 2001; Yan et al., 2015; Wang et al., 2017; Asmerom et al., 2020). Together, these changes in atmospheric–oceanic modes likely resulted in the northward migration of the EASM margin during warm periods, and vice versa during cold periods (Figs. 7 and 8).

It should be noted that ENSO is closely linked to equatorial Pacific SSTs, which are also controlled by solar irradiance (caused by the greater sensitivity of the western equatorial Pacific to radiative forcing relative to the eastern equatorial Pacific; see Rustic et al., 2015). This was the dominant modulator of precipitation changes in the EASM region during the late Holocene, via atmospheric circulation teleconnections on interannual to longer timescales, as shown by existing proxy records and climate modeling (e.g., Conroy et al., 2008; Chen et al., 2015b; Xu et al., 2016; Liu et al., 2019; Lan et al., 2020). For example, shifts to more or less El Niño–like conditions (Fig. 8e) spanning cold to warm periods should lead to a decrease in EASM intensity by changing the position of the WPSH (Chen et al., 2015b; Lan et al., 2020; Jiang et al., 2021).

Specifically, El Niño-like conditions could occur during cold periods, when radiative forcing is weak and a decreased zonal SST gradient in the ocean occurs owing to decreased SSTs in the western tropical Pacific (Stott et al., 2004; Rein et al., 2005; Conroy et al., 2009; Jian et al., 2022; Fig. 8). This would lead to a weakened EASM and reduced moisture transport from the low-latitude Pacific to northern China and the margin of the NETP owing to the southward migration of the WPSH (Hou et al., 2003; Zhang et al., 2008; Li et al., 2010; Tan et al., 2011; Liu et al., 2019), but increased precipitation in the Yangtze River valley region. During warm periods, when radiative forcing was strong, this situation was reversed (Tong et al., 1997; He et al., 2003; Man, 2009). In summary, we argue that EASM intensity was dramatically enhanced (diminished) during warm (cold) periods, which may have primarily been a response to both the external forcing of strong (weak) total solar irradiance and the associated changes in atmospheric–oceanic modes, including internal forcing factors like the northern (southern) shift of the ITCZ and WPSH. La Niña-like (El Niño-like) conditions linked to an increased (decreased) tropical Pacific SST gradient resulted in increased (decreased) precipitation on the margin of the NETP and in northern China over the past 3500 years.

6. Conclusion

We have produced a reliably-dated quantitative multi-proxy paleoclimatic reconstructions for the late Holocene sediments of Lake Bihu, an alpine lake on the NETP. The record spans the last ~3500 years and the average sedimentation rate of ~0.63 mm/yr is sufficient to resolve climate variations on decadal to centennial timescales. High-resolution reconstructions of precipitation and quantitative mean air temperature are based on XRF-scanning element contents, grain-size, organic and silicate contents, and brGDGTs. The regional MAF reconstruction values ranged between 0.70 and 3.98 °C, with an average of 2.19 °C. Precipitation and temperature optima on the NETP occurred during the MWP, rather than during the CWP. Comparison of our precipitation and paleotemperature reconstructions with other local and global climate records indicate that notable and spatially extensive warm–wet climatic conditions occurred during the periods of 1500–900 BCE, RWP (250 BCE–450 CE), MWP (800–1400 CE), and CWP (1850–present); and relatively cold–dry climatic conditions during the intervals of 900–250 BCE, the DACP (450–800 CE), and LIA (1400–1800 CE), across the NETP region. The late Holocene temperature fluctuations on the NETP were primarily controlled by total solar irradiance, interrupted by successive volcanic eruptions, on a multidecadal timescale. The anomalous and rapid warming during the CWP could also be related to the unprecedented increase in atmospheric greenhouse gases during the 20th century. Precipitation, driven by EASM intensity, decreased substantially during cold periods, and it increased during warm periods; this may primarily have been a response to both the external forcing factor of total solar irradiance and the associated changes in atmospheric–oceanic modes. Specifically, when the zonal SST gradient in the tropical Pacific increases (decreases), owing to an increased (decreased) SST in the western tropical Pacific, the eastern tropical Pacific becomes dominated by a La Niña-like (El Niño-like) state, triggered by the stronger (weaker) radiative forcing; this coincides with periods of northward (southward) migration of both the ITCZ and WPSH, resulting in enhanced (diminished) precipitation in northern China and on the margin of the NETP region during historical warm (cold) periods. Overall, the climatic record from Lake Bihu is a unique dataset that can be used to understand temperature and precipitation patterns and their potential climate forcing mechanisms during the late Holocene, and to provide a reference frame for predicting future climate change over the Tibetan Plateau.

Declaration of Competing Interest

The authors declare that they have no known competing financial interests or personal relationships that could have appeared to influence the work reported in this paper.

Data availability

Data will be made available on request.

Acknowledgements

This research was supported by National Natural Science Foundation of China (42171150), and Second Tibetan Plateau Scientific Expedition and Research Program (STEP) (2019QZKK0601).

Appendix A. Supplementary data

Supplementary data to this article can be found online at https://doi.org/10.1016/j.palaeo.2023.111442.

References

An, F.Y., Lai, Z.P., Liu, X.J., Wang, Y.X., Chang, Q.F., Lu, B.L., Yang, X.Y., 2018. Luminescence chronology and radiocarbon reservoir age determination of lacustrine sediments from the Heihai Lake, NE Qinghai-Tibetan Plateau and its paleoclimate implications. J. Earth Sci. China 29 (3), 695–706.

An, Z.S., Colman, S.M., Zhou, W.J., Li, X.Q., Brown, E.T., Jull, A.J.T., Cai, Y.J., Huang, Y. S., Lu, X.F., Chang, H., Song, Y.G., Sun, Y.B., Xu, H., Liu, W.G., Jin, Z.D., Liu, X.D., Cheng, P., Liu, Y., Ai, L., Li, X.Z., Liu, X.J., Yan, L.B., Shi, Z.G., Wang, X.L., Wu, F., Qiang, X.K., Dong, J.B., Lu, F.Y., Xu, X.W., 2012. Interplay between the Westerlies and Asian monsoon recorded in Lake Qinghai sediments since 32 ka. Sci. Rep. 2, 619.

Asmerom, Y., Baldini, J.U.L., Prufer, K.M., Polyak, V.J., Ridley, H.E., Poliak, Aquino V., Baldini, L.M., Breitenbach, S.F.M., Macpherson, C.G., Kennett, D.J., 2020. Intertropical convergence zone variability in the Neotropics during the Common Era. Sci. Adv. 6 (7), eaax3644.

Blaauw, M., 2010. Methods and code for 'classical' age modeling of radiocarbon sequences. Quat. Geochronol. 5, 512–518.

Brierley, C.M., Zhao, A.N., Harrison, S.P., Braconnot, P., Williams, C.J.R., Thornalley, D. J.R., Thorn, Shi X., Alley, Peterschmitt J.Y., Ohgaito, R., Kaufman, D.S., Kageyama, M., Hargreaves, J.C., Erb, M.P., Emile-Geay, J., D'Agostino, R., Chandan, D., Carre, M., Bartlein, P.J., Zheng, W.P., Zhang, Z.S., Zhang, Q., Yang, H., Volodin, E.M., Tomas, R.A., Routson, C., Peltier, W.R., Otto-Bliesner, B., Morozova, P.A., McKay, N.P., Lohmann, G., Legrande, A.N., Guo, C.C., Cao, J.,

Brady, E., Annan, J.D., Abe-Ouchi, A., 2020. Large-scale features and evaluation of the PMIP4-CMIP6 mid-Holocene simulations. Clim. Past. Disc. 16 (5), 1847–1872.
Briffa, K.R., Melvin, T.M., Osborn, T.J., Hantemirov, R.M., Kirdyanov, A.V., Mazepa, V. S., Shiyatov, S.G., Esper, J., 2013. Reassessing the evidence for tree-growth and inferred temperature change during the Common Era in Yamalia, Northwest Siberia. Quat. Sci. Rev. 72, 83–107.
Cao, J., Rao, Z., Shi, F., Jia, G., 2020. Ice formation on lake surfaces in winter causes warm-season bias of lacustrine brGDGT temperature estimates. Biogeosciences 17, 2521–2536.
Castellano, E., Becagli, S., Hansson, M., Hutterli, M., Petit, J.R., Rampino, M.R., Severi, M., Steffensen, J.P., Traversi, R., Udisti, R., 2005. Holocene volcanic history as recorded in the sulfate stratigraphy of the European Project for Ice Coring in Antarctica Dome C (EDC96) ice core. J. Geophys. Res. 110, D06114.
Chen, J.H., Chen, F.H., Feng, S., Huang, W., Liu, J.B., Zhou, A.F., 2015b. Hydroclimatic changes in China and surroundings during the Medieval Climate Anomaly and Little Ice Age: spatial patterns and possible mechanisms. Quat. Sci. Rev. 107, 98–111.
Chen, F.H., Chen, J.H., Holmes, J., Boomer, I., Austin, P., Gates, J.B., Wang, N.L., Brooks, S.J., Zhang, J.W., 2010. Moisture changes over the last millennium in arid Central Asia: a review, synthesis and comparison with monsoon region. Quat. Sci. Rev. 29 (7–8), 1055–1068.
Chen, F.H., Huang, X.Z., Zhang, J.W., Holmes, J.A., Chen, J.H., 2006. Humid little ice age in arid Central Asia documented by Bosten Lake,Xinjiang. Sci. China Ser. D 49 (12), 1280–1290.
Chen, F.H., Wu, D., Chen, J.H., Zhou, A.F., Yu, J.Q., Shen, J., Wang, S.M., Huang, X.Z., 2016. Holocene moisture and East Asian summer monsoon evolution in the northeastern Tibetan Plateau recorded by Lake Qinghai and its environs: a review of conflicting proxies. Quat. Sci. Rev. 154, 111–129.
Chen, J.A., Wan, G.J., Zhang, F., Huang, R.G., 2003. The record of lake sediments in different scales-taking grain size for example. Sci. China B 33 (6), 563–5683.
Chang, J., Zhang, E.L., Liu, E.F., Shulmeister, J., 2017. Summer temperature variability inferred from subfossil chironomid assemblages from the south-east margin of the Qinghai-Tibetan plateau for the last 5000 years. The Holocene 27 (12), 1876–1884.
Chen, L., Huang, Z.D., Niu, L.L., Dong, W.M., Xiao, S., Chen, S.Q., Zhao, J.J., Wu, D., Zhou, A.F., 2021. GDGTs-based quantitative reconstruction of water level changes and precipitation at Daye Lake, Qinling Mountains (central-East China), over the past 2000 years. Quat. Sci. Rev. 267, 107099.
Chen, D.L., Xu, B.Q., Yao, T.D., 2015a. Assessment of past, present and future environmental changes on the Tibetan Plateau. Chin. Sci. Bull. 1–11 (in Chinese).
Chylek, P., Folland, C.K., Lesins, G., Dubey, M.K., Wang, M.Y., 2009. Arctic air temperature change amplification and the Atlantic Multidecadal Oscillation. Geophys. Res. Lett. 36, L14801.
Conroy, J.L., Overpeck, J.T., Cole, J.E., Shanahan, T.M., Steinitz-Kannan, M., 2008. Holocene changes in eastern tropical Pacific climate inferred from a Galapagos lake sediment record. Quat. Sci. Rev. 27 (11–12), 1166–1180.
Conroy, J.L., Restrepo, A., Overpeck, J.T., Steinitz-Kannan, M., Cole, J.E., Bush, M.B., Colinvaux, P.A., 2009. Unprecedented recent warming of surface temperatures in the eastern tropical Pacific Ocean. Nat. Geosci. 2 (1), 46–50.
Crowley, T.J., 2000. Causes of climate change over the past 1000 years. Science 289 (5477), 270–277.
Dang, X.Y., Ding, W.H., Yang, H., Pancost, R.D., Naafs, B.D.A., Xue, J.T., Lin, X., Lu, J.Y., Xie, S.C., 2018. Different temperature dependence of the bacterial brGDGT isomers in 35 Chinese lake sediments compared to that in soils. Org. Geochem. 119, 72–79.
De Jonge, C., Hopmans, E.C., Zell, C.I., Kim, J.-H., Schouten, S., Sinninghe Damsté, J.S., 2014. Occurrence and abundance of 6-methyl branched glycerol dialkyl glyc-erol tetraethers in soils: implications for palaeoclimate reconstruction. Geochim. Cosmochim. Acta 141, 97–112.
De Jonge, C., Stadnitskaia, A., Fedotov, A., Damsté, J.S.S., 2015a. Impact of riverine suspended particulate matter on the branched glycerol dialkyl glycerol tetraether composition of lakes: the outflow of the Selenga River in Lake Baikal (Russia). Org. Geochem. 83–84, 241–252.
De Jonge, C., Stadnitskaia, A., Hopmans, E.C., Cherkashov, G., Fedotov, A., Streletskaya, I.D., Vasiliev, A.A., Damste, J.S.S., 2015b. Drastic changes in the distribution of branched tetraether lipids in suspended matter and sediments from the Yenisei River and Kara Sea (Siberia): implications for the use of brGDGT-based proxies in coastal marine sediments. Geochim. Cosmochim. Acta 165, 200–225.
Dean, W.E., 1974. Determination of carbonate and organic matter in calcareous sediments and sedimentary rocks by loss on ignition; comparison with other methods. J. Sediment. Res. 44, 242–248.
Dearing Crampton-Flood, E., Tierney, J.E., Peterse, F., Kirkels, F.M.S.A., Sinninghe Damsté, J.S., 2020. BayMBT: a Bayesian calibration model for branched glycerol dialkyl glycerol tetraethers in soils and peats. Geochim Cosmochim Ac 268, 142–159.
Deng, L.H., Jia, G.D., Jin, C.F., Li, S.J., 2016. Warm season bias of branched GDGT temperature estimates causes underestimation of altitudinal lapse rate. Org. Geochem. 96, 11–17.
Diaz, H.F., Trigo, R., Hughes, M.K., Mann, M.E., Xoplaki, E., Barriopedro, D., 2011. Spatial and temporal characteristics of climate in medieval times revisited. Bull. Am. Meteorol. Soc. 92, 1487–1500.
Ding, Q.H., Wang, B., 2005. Circumglobal teleconnection in the Northern Hemisphere summer. J. Clim. 18 (17), 3483–3505.
Ding, S., Xu, Y., Wang, Y., He, Y., Hou, J., Chen, L., He, J.S., 2015. Distribution of branched glycerol dialkyl glycerol tetraethers in surface soils of the Qinghai-Tibetan Plateau: implications of brGDGTs-based proxies in cold and dry regions. Biogeosciences 12 (11), 3141–3151.
Feng, X.P., Zhao, C., D'Andrea, W.J., Hou, J.Z., Yang, X.D., Xiao, X.Y., Shen, J., Duan, Y. W., Chen, F.H., 2022. Evidence for a relatively warm mid-to late Holocene on the southeastern Tibetan Plateau. Geophys. Res. Lett. 49, e2022GL098740.
Feng, X.P., Zhao, C., D'Andrea, W.J., Liang, J., Zhou, A.F., Shen, J., 2019. Temperature fluctuations during the Common Era in subtropical southwestern China inferred from brGDGTs in a remote alpine lake. Earth Planet. Sci. Lett. 510, 26–36.
Ge, Q.S., Zheng, J.Y., Hao, Z.X., Liu, H.L., 2013. General characteristics of climate changes during the past 2000 years in China. Sci. China Earth Sci. 56 (2), 321–329.
Ge, Q.S., Zheng, J.Y., Hao, Z.X., Shao, X.M., Wang, W.C., Luterbacher, J., 2010. Temperature variation through 2000 years in China: an uncertainty analysis of reconstruction and regional difference. Geophys. Res. Lett. 37, L03703.
Günther, F., Thiele, A., Gleixner, G., Xu, B.Q., Yao, T.D., Schouten, S., 2014. Distribution of bacterial and archaeal ether lipids in soils and surface sediments of Tibetan lakes: implications for GDGT-based proxies in saline high mountain lakes. Org. Geochem. 67, 19–30.
Haug, G.H., Hughen, K.A., Sigman, D.M., Peterson, L.C., Rohl, U., 2001. Southward migration of the intertropical convergence zone through the Holocene. Science 293 (5533), 1304–1308.
He, Y.X., Liu, W.G., Zhao, C., Wang, Z., Wang, H.Y., Liu, Y., Qin, X.Y., Hu, Q.H., An, Z.S., Liu, Z.H., 2013b. Solar influenced late Holocene temperature changes on the northern Tibetan Plateau. Chin. Sci. Bull. 58 (9), 1053–1059.
He, Y.X., Zhao, C., Wang, Z., Wang, H.Y., Song, M., Liu, W.G., Liu, Z.H., 2013a. Late Holocene coupled moisture and temperature changes on the northern Tibetan Plateau. Quat. Sci. Rev. 80, 47–57.
He, Y., Hou, J.Z., Wang, M.D., Li, X.M., Liang, J., Xie, S.Y., Jin, Y.R., 2020. Temperature variation on the central Tibetan plateau revealed by glycerol dialkyl glycerol tetraethers from the sediment record of Lake Linggo Co since the last deglaciation. Front. Earth Sci. 8, 574206.
He, B.Y., Zhang, S., Cai, S.M., 2003. Climatic changes recorded in peat from the Dajiu Lake basin in Shennongjia since the last 2600 years. Mar. Geol. Quat. Geol. 23, 109–115 (in Chinese).
Heiri, O., Lotter, A.F., Lemcke, G., 2001. Loss on ignition as a method for estimating organic and carbonate content in sediments: reproducibility and comparability of results. J. Paleolimnol. 25 (1), 101–110.
Hopmans, E.C., Schouten, S., Damsté, J.S.S., 2016. The effect of improved chromatography on GDGT-based palaeoproxies. Org. Geochem. 93, 1–6.
Hopmans, E.C., Weijers, J.W.H., Schefuß, E., Herfort, L., Damsté, J.S.S., Schouten, S., 2004. A novel proxy for terrestrial organic matter in sediments based on branched and isoprenoid tetraether lipids. Earth Planet. Sci. Lett. 107, 26–116.
Hou, G.L., Chongyi, E.Y., Liu, X.J., Zeng, F.M., 2013. Reconstruction of integrated temperature series of the past 2,000 years on the tibetan plateau with 10-year intervals. Theor. Appl. Climatol. 113 (1–2), 259–269.
Hou, J.Z., Huang, Y.S., Zhao, J.T., Liu, Z.H., Colman, S., An, Z.S., 2016. Large Holocene summer temperature oscillations and impact on the peopling of the northeastern Tibetan Plateau. Geophys. Res. Lett. 43, 1323–1330.
Hou, J.Z., Tan, M., Cheng, H., Liu, T.S., 2003. Stable isotope records of plant cover change and monsoon variation in the past 2200 years: evidence from laminated stalagmites in Beijing,China. Boreas 32 (2), 304–313.
Hu, J.F., Zhou, H.D., Peng, P.A., Spiro, B., 2016. Seasonal variability in concentrations and fluxes of glycerol dialkyl glycerol tetraethers in Huguangyan Maar Lake, SE China: implications for the applicability of the MBT-CBT paleotemperature proxy in lacustrine settings. Chem. Geol. 420, 200–212.
Immerzeel, W.W., van Beek, L.P.H., Bierkens, M.F.P., 2010. Climate change will affect the Asian. Science 328 (5984), 1382–1385.
IPCC, 2021. Climate Change 2021: The Physical Science Basis. In: Masson-Delmotte, V., et al. (Eds.), Contribution of Working Group I to the Sixth Assessment Report of the Intergovernmental Panel on Climate Change. Cambridge University Press, London.
Jian, Z., Qiang, L., Li, T.-Y., Chaojun, C., Li, J., 2022. Asian-australian monsoon evolution over the last millennium linked to ENSO in composite stalagmite $\delta^{18}O$ records. Quat. Sci. Rev. 281, 107420.
Jiang, S.W., Zhou, X., Sachs, J.P., Luo, W.H., Tu, L.Y., Liu, X.Q., Zeng, L.Y., Peng, S.Z., Yan, Q., Liu, F., Zheng, J.Q., Zhang, J.Z., Shen, Y.A., 2021. Central eastern China hydrological changes and ENSO-like variability over the past 1800 yr. Geology 49 (11), 1386–1390.
Jin, Z.D., An, Z.S., Yu, J.M., Li, F.C., Zhang, F., 2015. Lake Qinghai sediment geochemistry linked to hydroclimate variability since the last glacial. Quat. Sci. Rev. 122, 63–73.
Kylander, M.E., Ampel, L., Wohlfarth, B., Veres, D., 2011. High-resolution X-ray fluorescence core scanning analysis of LesEchets (France) sedimentary sequence: new insights fromchemical proxies. J. Quat. Sci. 26, 109–117.
Lan, J.H., Xu, H., Lang, Y.C., Yu, K.K., Zhou, P., Kang, S.G., Zhou, K.G., Wang, X.L., Wang, T.L., Cheng, P., Yan, D.N., Yu, S.Y., Che, P., Ye, Y.D., Tan, L.C., 2020. Dramatic weakening of the East Asian summer monsoon in northern China during the transition from the medieval warm period to the Little Ice Age. Geology 48 (4), 307–312.
Li, H.M., Dai, A.G., Zhou, T.J., Lu, J., 2010. Responses of East Asian summer monsoon to historical SST and atmospheric forcing during 1950–2000. Clim. Dyn. 34 (4), 501–514.
Li, J.J., Pan, B.T., 1989. In: Quaternary glaciation in the Daligia Mountain on the northeast border of Qinghai–Xizang Plateau. International Field Workshop on Loess Geomor-phological Processes and Hazards. J Lanzhou Univ, pp. 101–108.
Li, X.M., Wang, M.D., Hou, J.Z., 2019. Centennial-scale climate variability during the past 2000 years derived from lacustrine sediment on the western Tibetan Plateau. Quat. Int. 510, 65–75.
Li, X.M., Wang, M.D., Zhang, Y.Z., Lei, L., Hou, J.Z., 2017. Holocene climatic and environmental change on the western Tibetan Plateau revealed by glycerol dialkyl

glycerol tetraethers and leaf wax deuterium-to-hydrogen ratios at Aweng Co. Quat. Res. 87 (3), 455–467.
Li, X.M., Zhang, Y., Hou, J.Z., Wang, M.D., Fan, B.W., Yan, J.H., Huang, L.X., He, Y., 2022. Spatio-temporal patterns of centennial-scale climate change over the Tibetan Plateau during the past two millennia and their possible mechanisms. Quat. Sci. Rev. 292, 107664.
Li, X.M., Zhang, Y., Wang, M.D., Yan, I.H., Fan, B.W., Xing, W., He, Y., Hou, J.Z., 2020. Centennialscale temperature change during the Common Era revealed by quantitative temperature reconstructions on the Tibetan Plateau. Front. Earth Sci. 8, 360.
Li, Y.M., Wu, D., Yuan, Z.J., Chen, L., Chen, X.M., Zhou, A.F., 2022. Holocene summer monsoon variation and environmental response in the drainage basin of Lake Bande in the inner Tibetan Plateau. Quat. Sci. 42 (5), 1328–1348 (in Chinese).
Li, Y., Zhao, S.J., Pei, H.Y., Qian, S., Zang, J.J., Dang, X.Y., Yang, H., 2018. Distribution of glycerol dialkyl glycerol tetraethers in surface soils along an altitudinal transect at cold and humid Mountain Changbai: implications for the reconstruction of paleoaltimetry and paleoclimate. Sci. China Earth Sci. 61, 925–939.
Liu, B., Sheng, E.G., Yu, K.K., Zhou, K.E., Lan, J.H., 2022. Variations in monsoon precipitation over Southwest China during the last 1500 years and possible driving forces. Sci. China Earth Sci. 65 (5), 949–965.
Liu, J.B., Chen, F.H., Chen, J.H., Xia, D.S., Xu, Q.H., Wang, Z.L., Li, Y.C., 2011a. Humid medieval warm period recorded by magnetic characteristics of sediments from Gonghai Lake, Shanxi,North China. Chin. Sci. Bull. 56 (23), 2464–2474.
Liu, H.Y., Gu, Y.S., Huang, X.Y., Yu, Z.C., Xie, S.C., Cheng, S.G., 2019. A 13,000-year peatland palaeohydrological response to the ENSO-related Asian monsoon precipitation changes in the middle Yangtze Valley. Quat. Sci. Rev. 212, 80–91.
Liu, X.D., Chen, B.D., 2000. Climatic warming in the Tibetan Plateau during recent decades. Int. J. Climatol. 20, 1729–1742.
Liu, X.X., Vandenberghe, J., An, Z.S., Li, Y., Jin, Z.D., Dong, J.B., Sun, Y.B., 2016. Grain size of Lake Qinghai sediments: implications for riverine input and Holocene monsoon variability. Palaeogeogr. Palaeoclimatol. Palaeoecol. 449, 41–51.
Liu, X., Shao, X., Zhao, L., et al., 2007. Dendron climatic temperature record derived from tree-ring width and stable carbon isotope chronologies in the Middle Qilian Mountains, China. Arctic Antarct Alpine Res. 39, 651–657.
Liu, Y., An, Z.S., Linderholm, H.W., Chen, D.L., Song, H.M., Cai, Q.F., Sun, J.Y., Tian, H., 2009. Annual temperatures during the last 2485 years in the mid-eastern Tibetan Plateau inferred from tree rings. Sci. China Series D 52 (3), 348–359.
Liu, Z.H., Henderson, A.C.G., Huang, Y.S., 2006. Alkenone-based reconstruction of late-Holocene surface temperature and salinity changes in Lake Qinghai,China, 33, L09707.
Liu, J.A., Wang, B., Wang, H.L., Kuang, X.Y., Ti, R.Y., 2011b. Forced response of the East Asian summer rainfall over the past millennium: results from a coupled model simulation. Clim. Dyn. 36 (1–2), 323–336.
Liu, Z.Y., Zhu, J., Rosenthal, Y., Zhang, X., Otto-Bliesner, B.L., Timmermann, A., Smith, R.S., Lohmann, G., Zheng, W.P., Timm, O.E., 2014. The Holocene temperature conundrum. Proc. Natl. Acad. Sci. U. S. A. 111 (34), E3501–E3505.
Ljungqvist, F.C., 2010. A new reconstruction of temperature variability in the extra-tropical Northern Hemisphere during the last two millennia. Geogr. Ann. A 92a (3), 339–351.
Ma, X.Y., Wu, D., Liang, Y., Yuan, Z.J., Wang, T., Li, Y.M., 2022. Changes in regional religious activities in the last millennium recorded by black carbon in Lake Dalzong, northeastern Tibetan Plateau. Sci. China Earth Sci. 66, 1–13.
Mahaney, W.C., Rutter, N.W., 1992. Relative ages of the moraines of the Dalijia Shan, Northwestern China. Catena 19 (2), 179–191.
Makou, M.C., Eglinton, T.I., Oppo, D.W., Hughen, K.A., 2010. Postglacial changes in El Niño and La Niña behavior. Geology 38 (1), 43–46.
Man, Z.M., 2009. Research on Climate Change during Historical Times in China. Shandong Education Press, Ji'nan.
Mann, M.E., Fuentes, J.D., Rutherford, S., 2012. Underestimation of volcanic cooling in tree-ring-based reconstructions of hemispheric temperatures. Nat. Geosci. 5 (3), 202–205.
Mann, M.E., Zhang, Z.H., Rutherford, S., Bradley, R.S., Hughes, M.K., Shindell, D., Ammann, C., Faluvegi, G., Ni, F.B., 2009. Global signatures and dynamical origins of the little ice ageand medieval climate anomaly. Science 326 (5957), 1256–1260.
Marcott, S.A., Shakun, J.D., Clark, P.U., Mix, A.C., 2013. A reconstruction of regional and global temperature for the past 11,300 years. Science 339 (6124), 1198–1201.
Martínez-Sosa, P., Tierney, J.E., Stefanescu, I.C., Crampton-Flood, E.D., Shuman, B.N., Routson, C., 2021. A global Bayesian temperature calibration for lacustrine brGDGTs. Geochim. Cosmochim. Acta 305, 87–105.
Moberg, A., Sonechkin, D.M., Holmgren, K., Datsenko, N.M., Karlen, W., 2005. Highly variable Northern Hemisphere temperatures reconstructed from low- and high-resolution proxy data. Nature 433 (7026), 613–617.
Naafs, B.D.A., Inglis, G.N., Zheng, Y., Amesbury, M.J., Biester, H., Bindler, R., Blewett, J., Burrows, M.A., Torres, D.D., Chambers, F.M., Cohen, A.D., Evershed, R.P., Feakins, S.J., Galka, M., Gallego-Sala, A., Gandois, L., Gray, D.M., Hatcher, P.G., Coronado, E.N.H., Hughes, P.D.M., Huguet, A., Kononen, M., Laggoun-Defarge, F., Lahteenoja, O., Lamentowicz, M., Marchant, R., McClymont, E., Pontevedra-Pombal, X., Ponton, C., Pourmand, A., Rizzuti, A.M., Rochefort, L., Schellekens, J., De Vleeschouwer, F., Pancost, R.D., 2017. Introducing global peat-specific temperature and pH calibrations based on brGDGT bacterial lipids. Geochim. Cosmochim. Acta 208, 285–301.
Ning, D.L., Zhang, E.L., Shulmeister, J., Chang, J., Sun, W.W., Ni, Z.Y., 2019. Holocene mean annual air temperature (MAAT) reconstruction based on branched glycerol dialkyl glycerol tetraethers from Lake Ximenglongtan, southwestern China. Org. Geochem. 133, 65–76.
Olsson, I., 1986. Radiometric methods. In: Berglund, B. (Ed.), Handbook of Holocene Palaeoecology and Palaeohydrology. John Wiley and Sons, Chichester, pp. 273–312.
Pan, B.T., 1993. Quaternary glaciations on the Dalijia Shan. In: Chen, F.H., Zhang, W.X. (Eds.), Loess Stratigraphy and Quaternary Glaciations in the Gansu and Qinghai Provinces. Science Press, Beijing, pp. 96–103 (in Chinese).
PAGES 2k Consortium, 2017. A global multiproxy database for temperature reconstructions of the Common Era. Sci. Data 4, 170088.
Pei, H.Y., Wang, C.F., Wang, Y.B., Yang, H., Xie, S.C., 2019. Distribution of microbial lipids at an acid mine drainage site in China: insights into microbial adaptation to extremely low pH conditions. Org. Geochem. 134, 77–91.
Peng, J., Yang, X.Q., Toney, J.L., Ruan, J.Y., Li, G.H., Zhou, Q.X., Gao, H.H., Xie, Y.X., Chen, Q., Zhang, T.W., 2019. Indian Summer Monsoon variations and competing influences between hemispheres since similar to 35 ka recorded in Tengchongqinghai Lake, southwestern China. Palaeogeogr. Palaeoclimatol. Palaeoecol. 516, 113–125.
Peng, Y.J., Xiao, J., Nakamura, T., Liu, B.L., Inouchi, Y., 2005. Holocene East Asian monsoonal precipitation pattern revealed by grain-size distribution of core sediments of Daihai Lake in Inner Mongolia of north-Central China. Earth Planet. Sci. Lett. 233 (3–4), 467–479.
Pepin, N., Bradley, R.S., Diaz, H.F., Baraer, M., Caceres, E.B., Forsythe, N., Fowler, H., Greenwood, G., Hashmi, M.Z., Liu, X.D., Miller, J.R., Ning, L., Ohmura, A., Palazzi, E., Rangwala, I., Schoner, W., Severskiy, I., Shahgedanova, M., Wang, M.B., Williamson, S.N., Yang, D.Q., Grp, M.R.I.E.W., 2015. Elevation-dependent warming in mountain regions of the world. Nat. Clim. Chang. 5 (5), 424–430.
Peterse, F., van der Meer, J., Schouten, S., Weijers, J.W.H., Fierer, N., Jackson, R.B., Kim, J.H., Sinninghe Damsté, J.S., 2012. Revised calibration of the MBT–CBT paleotemperature proxy based on branched tetraether membrane lipids in sur-face soils. Geochim. Cosmochim. Acta 96, 215–229.
Qian, S., Yang, H., Dong, C., Wang, Y.B., Wu, J., Pei, H.Y., Dang, X.Y., Lu, J.Y., Zhao, S.J., Xie, S.C., 2019. Rapid response of fossil tetraether lipids in lake sediments to seasonal environmental variables in a shallow lake in Central China: implications for the usHe of tetraether-based proxies. Org. Geochem. 128, 108–121.
Qiang, M.R., Liu, Y.Y., Jin, Y.X., Song, L., Huang, X.T., Chen, F.H., 2014. Holocene record of eolian activity from Genggahai Lake, northeastern Qinghai- Tibetan Plateau, China. Geophys. Res. Lett. 41 (2), 589–595.
Raberg, J.H., Harning, D.J., Crump, S.E., de Wet, G., Blumm, A., Kopf, S., Geirsdottir, A., Miller, G.H., Sepulveda, J., 2021. Revised fractional abundances and warm-season temperatures substantially improve brGDGT calibrations in lake sediments. Biogeosciences 18 (12), 3579–3603.
Raberg, J.H., Miller, G.H., Geirsdottir, A., Sepulveda, J., 2022. Near-universal trends in brGDGT lipid distributions in nature. Sci. Adv. 8 (20), 1–12.
Reimer, P.J., Austin, W.E.N., Bard, E., Bayliss, A., Blackwell, P.G., Bronk Ramsey, C., Butzin, M., Cheng, H., Edwards, R.L., Friedrich, M., Grootes, P.M., Guilderson, T.P., Hajdas, I., Heaton, T.J., Hogg, A.G., Hughen, K.A., Kromer, B., Manning, S.W., Muscheler, R., Palmer, J.G., Pearson, C., van der Plicht, J., Reimer, R.W., Richards, D.A., Scott, E.M., Southon, J.R., Turney, C.S.M., Wacker, L., Adolphi, F., Büntgen, U., Capano, M., Fahrni, S.M., Fogtmann-Schulz, A., Friedrich, R., Köhler, P., Kudsk, S., Miyake, F., Olsen, J., Reinig, F., Sakamoto, M., Sookdeo, A., Talamo, S., 2020. The IntCal20 northern hemi-sphere radiocarbon age calibration curve (0–55 cal kBP). Radiocarbon 62, 725–757.
Rein, B., Luckge, A., Reinhardt, L., Sirocko, F., Wolf, A., Dullo, W.C., 2005. El Niño variability off Peru during the last 20,000 years. Paleoceanography 20 (4), PA4003.
Russell, J.M., Hopmans, E.C., Loomis, S.E., Liang, J., Damsté, J.S.S., 2018. Distributions of 5-and 6-methyl branched glycerol dialkyl glycerol tetraethers (brGDGTs) in East African lake sediment: effects of temperature, pH, and new lacustrine paleotemperature calibrations. Org. Geochem. 117, 56–69.
Rustic, G.T., Koutavas, A., Marchitto, T.M., Linsley, B.K., 2015. Dynamical excitation of the tropical Pacific Ocean and ENSO variability by Little Ice Age cooling. Science 350 (6267), 1537–1541.
Salzer, M.W., Bunn, A.G., Graham, N.E., Hughes, M.K., 2014. Five millennia of paleotemperature from tree-rings in the Great Basin, USA. Clim. Dyn. 42 (5–6), 1517–1526.
Schouten, S., Hopmans, E.C., Damsté, J.S.S., 2013. The organic geochemistry of glycerol dialkyl glycerol tetraether lipids: a review. Org. Geochem. 54, 19–61.
Shanahan, T.M., Hughen, K.A., Van Mooy, B.A.S., 2013. Temperature sensitivity of branched and isoprenoid GDGTs in Arctic lakes. Org. Geochem. 64, 119–128.
Shao, X., Xu, Y., Yin, Z.Y., Liang, E., Zhu, H., Wang, S., 2010. Climatic implications of a 3585-year tree-ring width chronology from the northeastern Qinghai-Tibetan Plateau. Quat. Sci. Rev. 29 (17–18), 2111–2122.
Shen, J., Wu, X.D., Zhang, Z., Gong, W.M., He, T., Xu, X.M., Dong, H.L., 2013. Ti content in Huguangyan maar lake sediment as a proxy for monsoon-induced vegetation density in the Holocene. Geophys. Res. Lett. 40 (21), 5757–5763.
Shen, Y.P., Kang, J.C., Zilliacus, H., 1989. In: Correlation of the Ice Age and loess deposit sequence in the region of the Mount Dalijia, Gansu, China. International Field Workshop on Loess Geomorphological Processes and Hazards. J Lanzhou Univ, pp. 109–119.
Shi, H., Wang, B., 2019. How does the asian summer precipitation-ENSO relationship change over the past 544 years? Clim. Dyn. 52, 4583–4598.
Shi, H., Wang, B., Cook, E.R., Liu, J., Liu, F., 2018. Asian summer precipitation over the past 544 years reconstructed by merging tree rings and historical documentary records. J. Clim. 31 (19), 7845–7861.
Sigl, M., Winstrup, M., McConnell, J.R., Welten, K.C., Plunkett, G., Ludlow, F., Buntgen, U., Caffee, M., Chellman, N., Dahl-Jensen, D., Fischer, H., Kipfstuhl, S., Kostick, C., Maselli, O.J., Mekhaldi, F., Mulvaney, R., Muscheler, R., Pasteris, D.R., Pilcher, J.R., Salzer, M., Schupbach, S., Steffensen, J.P., Vinther, B.M., Woodruff, T.

E., 2015. Timing and climate forcing of volcanic eruptions for the past 2,500 years. Nature 523, 543–549.
Sinha, A., Kathayat, G., Cheng, H., Breitenbach, S.F.M., Berkelhammer, M., Mudelsee, M., Biswas, J., Edwards, R.L., 2015. Trends and oscillations in the Indian summer monsoon rainfall over the last two millennia. Nat. Commun. 6039.
Sinninghe Damsté, J.S., Ossebaar, J., Abbas, B., Schouten, S., Verschuren, D., 2009. Fluxes and distribution of tetraether lipids in an equatorial African lake: constraints on the application of the TEX86 palaeothermometer and BIT index in lacustrine settings. Geochim. Cosmochim. Acta 73, 4232–4249.
Steinhilber, F., Abreu, J.A., Beer, J., Brunner, I., Christl, M., Fischer, H., Heikkila, U., Kubik, P.W., Mann, M., McCracken, K.G., Miller, H., Miyahara, H., Oerter, H., Wilhelms, F., 2012. 9,400 years of cosmic radiation and solar activity from ice cores and tree rings. Proc. Natl. Acad. Sci. U. S. A. 109 (16), 5967–5971.
Stott, L., Cannariato, K., Thunell, R., Haug, G.H., Koutavas, A., Lund, S., 2004. Decline of surface temperature and salinity in the western tropical Pacific Ocean in the Holocene epoch. Nature 431 (7004), 56–59.
Sun, D.H., Bloemendal, J., Rea, D.K., Vandenberghe, J., Jiang, F.C., An, Z.S., Su, R.X., 2002. Grain-size distribution function of polymodal sediments in hydraulic and aeolian environments, and numerical partitioning of the sedimentary components. Sediment. Geol. 152, 263–277.
Sun, X.H., Zhao, C., Zhang, C., Feng, X.P., Yan, T.L., Yang, X.D., Shen, J., 2021. Seasonality in Holocene temperature reconstructions in southwestern China. Paleoceanogr. Paleoclimatol. 36, e2020PA004025.
Tan, L.C., Cai, Y.J., An, Z.S., Edwards, R.L., Cheng, H., Shen, C.C., Zhang, H.W., 2011. Centennial-to decadal-scale monsoon precipitation variability in the semi-humid region, northern China during the last 1860 years: records from stalagmites in Huangye Cave. The Holocene 21 (2), 287–296.
Tian, L., Masson-Delmotte, V., Stievenard, M., Yao, T., Jouzel, J., 2001. Tibetan Plateau summer monsoon northward extent revealed by measurements of water stable isotopes. J. Geophys. Res. 106, 28081–28088.
Tong, G.B., Shi, Y., Wu, R.J., Yang, X.D., Qu, W.C., 1997. Vegetation and climatic quantitative reconstruction of Longgan Lake since the past 3000 years. Mar. Geol. Quat. Geol. 17, 53–61 (in Chinese).
Toohey, M., Kruger, K., Sigl, M., Stordal, F., Svensen, H., 2016. Climatic and societal impacts of a volcanic double event at the dawn of the Middle Ages. Clim. Chang. 136 (3–4), 401–412.
Wang, H.Y., Dong, H.L., Zhang, C.L.L., Jiang, H.C., Liu, Z.H., Zhao, M.X., Liu, W.G., 2015. Deglacial and Holocene archaeal lipid-inferred paleohydrology and paleotemperature history of Lake Qinghai, northeastern Qinghai-Tibetan Plateau. Quat. Res. 83 (1), 116–126.
Wang, H.Y., Dong, H.L., Zhang, C.L., Jiang, H.C., Liu, W.G., 2016. A 12-kyr record of microbial branched and isoprenoid tetraether index in Lake Qinghai, northeastern Qinghai-Tibet Plateau: implications for paleoclimate reconstruction. Sci. China Earth Sci. 59 (5), 951–960.
Wang, H.Y., An, Z.S., Lu, H.X., Zhao, Z.H., Liu, W.G., 2020. Calibrating bacterial tetraether distributions towards in situ soil temperature and application to a loess-paleosol sequence. Quat. Sci. Rev. 231, 106172.
Wang, H.Y., Liu, W.G., 2021. Soil temperature and brGDGTs along an elevation gradient on the northeastern Tibetan Plateau: a test of soil brGDGTs as a proxy for paleoelevation. Chem. Geol. 566, 120079.
Wang, H.Y., Chen, W., Zhao, H., Cao, Y.N., Hu, J., Zhao, Z.H., Cai, Z.Y., Wu, S.G., Liu, Z. H., Liu, W.G., 2023. Biomarker-based quantitative constraints on maximal soil-derived brGDGTs in modern lake sediments. Earth Planet. Sci. Lett. 602, 117947.
Wang, Y.J., Cheng, H., Edwards, R.L., He, Y.Q., Kong, X.G., An, Z.S., Wu, J.Y., Kelly, M. J., Dykoski, C.A., Li, X.D., 2005. The Holocene Asian monsoon: links to solar changes and North Atlantic climate. Science 308 (5723), 854–857.
Wang, J., Cui, H., Harbor, J.M., Zheng, L.M., Yao, P., 2015. Mid-MIS3 climate inferred from reconstructing the Dalijia Shan ice cap, north-eastern Tibetan Plateau. J. Quat. Sci. 30 (6), 558–568.
Wang, J., Kassab, C., Harbor, J.M., Caffee, M.W., Cui, H., Zhang, G.L., 2013. Cosmogenic nuclide constraints on late Quaternary glacial chronology on the Dalijia Shan, northeastern Tibetan Plateau. Quat. Res. 79 (3), 439–451.
Wang, M.Y., Zong, Y.Q., Zheng, Z., Man, M.L., Hu, J.F., Tian, L.P., 2018. Utility of brGDGTs as temperature and precipitation proxies in subtropical China. Sci. Rep. 8, 194.
Wang, M.Y., Zheng, Z., Zong, Y.Q., Man, M.L., Tian, L., 2019. Distributions of soil branched glycerol dialkyl glycerol tetraethers from different climate regions of China. Sci. Rep. 9, 1–8.
Wang, M.D., Liang, J., Hou, J.Z., Hu, L., 2016. Distribution of GDGTs in lake surface sediments on the Tibetan Plateau and its influencing factors. Sci. China Earth Sci. 59 (5), 961–974.
Wang, M.D., Hou, J.Z., Duan, Y.W., Chen, J.H., Li, X.M., He, Y., Lee, S.Y., Chen, F.H., 2021. Internal feedbacks forced Middle Holocene cooling on the Qinghai-Tibetan Plateau. Boreas 50, 1116–1130.
Wang, P.X., Wang, B., Cheng, H., Fasullo, J., Guo, Z.T., Kiefer, T., Liu, Z.Y., 2017. The global monsoon across time scales: mechanisms and outstanding issues. Earth Sci. Rev. 174, 84–121.
Wu, D., Ma, X.Y., Yuan, Z.J., Hillman, A.L., Zhang, J.W., Chen, J.H., Zhou, A.F., 2022. Holocene hydroclimatic variations on the Tibetan Plateau: an isotopic perspective. Earth Sci. Rev. 104169.
Wu, J., Yang, H., Pancost, R.D., Naafs, B.D.A., Qian, S., Dang, X.Y., Sun, H.L., Pei, H.Y., Wang, R.C., Zhao, S.J., Xie, S.C., 2021. Variations in dissolved O_2 in a Chinese lake drive changes in microbial communities and impact sedimentary GDGT distributions. Chem. Geol. 579, 120348.
Wu, D., Zhou, A.F., Zhang, J.W., Chen, J.H., Li, G.Q., Wang, Q., Chen, L., Madsen, D., Abbott, M., Cheng, B., Chen, F.H., 2020. Temperature-induced dry climate in basins in the northeastern Tibetan Plateau during the early to middle Holocene. Quat. Sci. Rev. 237, 106311.
Weijers, J.W.H., Schouten, S., van den Donker, J.C., Hopmans, E.C., Damsté, J.S.S., 2007. Environmental controls on bacterial tetraether membrane lipid distribution in soils. Geochim. Cosmochim. Acta 71 (3), 703–713.
Wu, X., Dong, H.L., Zhang, C.L., Liu, X.Q., Hou, W.G., Zhang, J., Jiang, H.C., 2013. Evaluation of glycerol dialkyl glycerol tetraether proxies for reconstruction of the paleo-environment on the Qinghai-Tibetan Plateau. Org. Geochem. 61, 45–56.
Xia, H., Zhang, D.J., Wang, Q., Wu, D., Duan, Y.W., Chen, F.H., 2020. A study of the construction times of the ancient cities in Ganjia Basin, Gansu Province, China. J. Geogr. Sci. 30 (9), 1467–1480.
Xiao, J.L., Fan, J.W., Zhou, L., Zhai, D.Y., Wen, R.L., Qin, X.G., 2013. A model for linking grain-size component to lake level status of a modern clastic lake. J. Asian Earth Sci. 69, 149–158.
Xiao, J., Si, B., Zhai, D., Itoh, S., Lomtatidze, Z., 2008. Hydrology of Dali Lake in Central-Eastern Inner Mongolia and Holocene East Asian monsoon variability. J. Paleolimnol. 40 (1), 519–528.
Xu, H., Lan, J.H., Sheng, E.G., Liu, B., Yu, K.K., Ye, Y.D., Shi, Z.G., Cheng, P., Wang, X.L., Zhou, X.Y., Yeager, K.M., 2016. Hydroclimatic contrasts over Asian monsoon areas and linkages to tropical Pacific SSTs. Sci. Rep. 6, 33177.
Xu, H., Sheng, E.G., Lan, J.H., Liu, B., Yu, K.K., 2015. Limnological records of the climatic changes along the eastern margin of the Tibetan Plateau during the past 2,000 years and their global linkages. Bull. Mineral. Petrol. Geochem. 34, 257–268 (in Chinese).
Yan, H., Wei, W., Soon, W., An, Z.S., Zhou, W.J., Liu, Z.H., Wang, Y.H., Carter, R.M., 2015. Dynamics of the intertropical convergence zone over the western Pacific during the Little Ice Age. Nat. Geosci. 8 (4), 315–320.
Yan, Y.P., You, Q.L., Wu, F.Y., Pepin, N., Kang, S.C., 2020. Surface mean temperature from the observational stations and multiple reanalyses over the Tibetan Plateau. Clim. Dyn. 55 (9–10), 2405–2419.
Yancheva, G., Nowaczyk, R.N., Mingram, J., Dulski, P., Schettler, G., Negendank, J.F.W., Liu, J.Q., Sigman, D.M., Peterson, L.C., Haug, G.H., 2007. Influence of the intertropical convergence zone on the East Asianmonsoon. Nature 455, 74–77.
Yang, B., Achim, B., Shi, Y.F., 2003. Late Holocene temperature fluctuations on the Tibetan Plateau. Quat. Sci. Rev. 22 (21–22), 2335–2344.
Yang, B., Braeuning, A., Johnson, K.R., Shi, Y.F., 2002. General characteristics of temperature variation in China during the last two millennia. Geophys. Res. Lett. 29 (9), 1–4.
Yang, B., Qin, C., Wang, J.L., He, M.H., Melvin, T.M., Osborn, T.J., Briffa, K.R., 2014. A 3,500-year tree-ring record of annual precipitation on the northeastern Tibetan Plateau. Proc. Natl. Acad. Sci. U. S. A. 111 (8), 2903–2908.
Yang, B., Qin, C., Bräuning, A., Osborn, T.J., Trouet, V., Ljungqvist, F.C., Schneider, L., Esper, J., Grießinger, J., Büntgen, U., Rossi, S., Dong, G.H., Yan, M., Ning, L., Wang, J.L., Wang, X.F., Wang, X.M., Luterbacher, J., Cook, E.R., Stenseth, N.C., 2021. Long-term decrease in Asian monsoon rainfall and abrupt climate change events over the past 6,700 years. Proc. Natl. Acad. Sci. U. S. A. 118, e2102007118.
Yao, T.D., Bolch, T., Chen, D.L., Gao, J., Immerzeel, W., Piao, S., Su, F.G., Thompson, L., Wada, Y., Wang, L., Wang, T., Wu, G.J., Xu, B.Q., Yang, W., Zhang, G.Q., Zhao, P., 2022. The imbalance of the Asian water tower. Nat. Rev. Earth Env. 1–15.
Yao, T.D., Masson-Delmotte, V., Gao, J., Yu, W.S., Yang, X.X., Risi, C., Sturm, C., Werner, M., Zhao, H.B., He, Y., Ren, W., Tian, L., Shi, C.M., Hou, S.G., 2013. A review of climatic controls on $\delta^{18}O$ in precipitation over the Tibetan Plateau: observations and simulations. Rev. Geophys. 51, 525–548.
Yao, T.D., Thompson, L., Yang, W., Yu, W.S., Gao, Y., Guo, X.J., Yang, X.X., Duan, K.Q., Zhao, H.B., Xu, B.Q., Pu, J.C., Lu, A.X., Xiang, Y., Kattel, D.B., Joswiak, D., 2012. Different glacier status with atmospheric circulations in Tibetan Plateau and surroundings. Nat. Clim. Chang. 2 (9), 663–667.
Yao, T.D., Xue, Y.K., Chen, D.L., Chen, F.H., Thompson, L., Cui, P., Koike, T., Lau, W.K. M., Lettenmaier, D., Mosbrugger, V., Zhang, R.H., Xu, B.Q., Dozier, J., Gillespie, T., Gu, Y., Kang, S.C., Piao, S.L., Sugimoto, S., Ueno, K., Wang, L., Wang, W.C., Zhang, F., Sheng, Y.W., Guo, W.D., Ailikun, Yang X.X., Ma, Y.M., Shen, S.S.P., Su, Z. B., Chen, F., Liang, S.L., Liu, Y.M., Singh, V.P., Yang, K., Yang, D.Q., Zhao, X.Q., Qian, Y., Zhang, Y., Li, Q., 2019. Recent third pole's rapid warming accompanies cryospheric melt and water cycle intensification and interactions between monsoon and environment: multidisciplinary approach with observations, modeling, and analysis. B Am. Meteorol. Soc. 100 (3), 423–444.
You, Q.L., Cai, Z.Y., Pepin, N., Chen, D.L., Ahrens, B., Jiang, Z.H., Wu, F.Y., Kang, S.C., Zhang, R.N., Wu, T.H., Wang, P.L., Li, M.C., Zuo, Z.Y., Gao, Y.H., Zhai, P.M., Zhang, Y.Q., 2021. Warming amplification over the Arctic Pole and Third Pole: trends, mechanisms and consequences. Earth Sci. Rev. 217, 103625.
Zang, J.J., Lei, Y.Y., Yang, H., 2018. Distribution of glycerol ethers in Turpan soils: implications for use of GDGT-based proxies in hot and dry regions. Front. Earth Sci. 12, 862–876.
Zhang, C., Zhao, C., Yu, S.Y., Yang, X.D., Cheng, J., Zhang, X.J., Xue, B., Shen, J., Chen, F. H., 2022a. Seasonal imprint of Holocene temperature reconstruction on the Tibetan Plateau. Earth Sci. Rev. 226, 103927.
Zhang, C., Zhao, C., Zhou, A.F., Zhang, H.X., Liu, W.G., Feng, X.P., Sun, X.S., Yan, T.L., Leng, C.C., Shen, J., Chen, F.H., 2021. Quantification of temperature and precipitation changes in northern China during the "5000-year" Chinese history. Quat. Sci. Rev. 255, 106819.
Zhang, E.L., Zhao, C., Xue, B., Liu, Z.H., Yu, Z.C., Chen, R., Shen, J., 2017. Millennial-scale hydroclimate variations in Southwest China linked to tropical Indian Ocean since the Last Glacial Maximum. Geology 45 (5), 435–438.
Zhang, C.B., Wu, D., Chen, X.M., Yuan, Z.J., Chen, F.H., 2022b. A preliminary study of the strata and age of ancient agricultural terraces in the Ganjia Basin, northeastern Tibetan Plateau. Acta Geograph. Sin. 77 (1), 66–78 (in Chinese).

Zhang, G.Q., Yao, T.D., Xie, H.J., Yang, K., Zhu, L.P., Shum, C.K., Bolch, T., Yi, S., Allen, S., Jiang, L.G., Chen, W.F., Ke, C.Q., 2020. Response of Tibetan Plateau lakes to climate change: trends, patterns, and mechanisms. Earth Sci. Rev. 208, 103269.

Zhang, J.W., Jin, M., Chen, F.H., Battarbee, R.W., Henderson, A.C.G., 2003. High-resolution precipitation variations in the Northeast Tibetan Plateau over the last 800 years documented by sediment cores of Qinghai Lake. Chin. Sci. Bull. 48 (14), 1451–1456.

Zhang, P.Z., Cheng, H., Edwards, R.L., Chen, F.H., Wang, Y.J., Yang, X.L., Liu, J., Tan, M., Wang, X.F., Liu, J.H., An, C.L., Dai, Z.B., Zhou, J., Zhang, D.Z., Jia, J.H., Jin, L.Y., Johnson, K.R., 2008. A test of climate, sun, and culture relationships from an 1810-year Chinese. Science 322 (5903), 940–942.

Zhang, Q.B., Cheng, G.D., Yao, T.D., Kang, X.C., Huang, J.G., 2003. A 2,326-year tree-ring record of climate variability on the northeastern Qinghai-Tibetan Plateau. Geophys. Res. Lett. 30 (14). HLS 2–1.

Zhang, J., Liang, M.Q., Li, T.Y., Chen, C.J., Li, J.Y., 2022c. Asian-Australian monsoon evolution over the last millennium linked to ENSO in composite stalagmite $\delta^{18}O$ records. Quat. Sci. Rev. 281, 107420.

Zhang, Y., Shao, X.M., Yin, Z.Y., Wang, Y., 2014. Millennial minimum temperature variations in the Qilian Mountains, China: evidence from tree rings. Clim. Past Discuss. 10, 1763–1778.

Zhao, C., Liu, Z.H., Rohling, E.J., Yu, Z.C., Liu, W.G., He, Y.X., Zhao, Y., Chen, F.H., 2013. Holocene temperature fluctuations in the northern Tibetan Plateau. Quat. Res. 80 (1), 55–65.

Zhao, C., Rohling, E.J., Liu, Z.Y., Yang, X.Q., Zhang, E.L., Cheng, J., Liu, Z.H., An, Z.S., Yang, X.D., Feng, X.P., Sun, X.S., Zhang, C., Yan, T.L., Long, H., Yan, H., Yu, Z.C., Liu, W.G., Yu, S.Y., Shen, J., 2021. Possible obliquity-forced warmth in southern Asia during the last glacial stage. Sci. Bull. 66, 1136–1145.

Zhao, J.J., Huang, Y.S., Yao, Y., An, Z.S., Zhu, Y.Z., Lu, H.X., Wang, Z., 2020. Calibrating branched GDGTs in bones to temperature and precipitation: application to Alaska chronological sequences. Quat. Sci. Rev. 240, 106371.

Zhu, H.F., Zheng, Y.H., Shao, X.M., Liu, X.H., Xu, Y., Liang, E.Y., 2008. Millennial temperature reconstruction based on tree-ring widths of Qilian juniper from Wulan, Qinghai Province,China. Chin. Sci. Bull. 53 (24), 1835–1841.

View publication stats